J. Fluid Mech. (1989), *vol.* 198, *pp.* 471–511
Printed in Great Britain

Nonlinear dynamics in Langmuir circulations and in thermosolutal convection

By SIDNEY LEIBOVICH†, SANJIVA K. LELE‡ AND IRENE M. MOROZ‖

† Sibley School of Mechanical and Aerospace Engineering, Cornell University, Ithaca, NY 14853-7501, USA

‡ NASA Ames Research Center, 202A-1, Moffett Field, CA 94035, USA

‖ School of Mathematics and Physics, University of East Anglia, Norwich, Norfolk NR4 7TJ, UK

(Received 15 December 1987 and in revised form 18 March 1988)

Two-dimensional motions generated by Langmuir circulation instability of stratified layers of water of finite depth are studied under a simplifying assumption making it mathematically analogous to double-diffusive thermosolutal convection with constant solute concentration and constant heat flux at the boundaries. The nature of possible motions is mapped over a significant region in (S, R) parameter space, where S and R are parameters measuring, respectively, the stabilizing and destabilizing agencies in the problem. In the Langmuir circulation problem R measures the effects of wind and surface wave action, and S measures the stabilizing effect of buoyancy: in the thermosolutal problem, R measures the destabilizing effects of heating, while S measures the stabilizing effect of solute concentration. Effects of lateral boundary or symmetry conditions are found to be crucial in determining the qualitative behaviour. Complex temporal behaviour, including intermittently chaotic flows, are found under suitably constrained (no flux) lateral conditions but are unstable and not realized when these constraints are relaxed and replaced by periodic lateral conditions. Multiple steady states also arise, with those found under constrained lateral conditions losing stability either to travelling waves, or to other steady states when the lateral boundary conditions are relaxed. In some regions of the parameter space, multiple stable nonlinear motions have been found under periodic boundary conditions. The multiple stable states may either be coexisting travelling waves and steady states (different from those found under the constrained lateral conditions). The existence of robust travelling waves may explain some field observations of laterally drifting windrows associated with Langmuir circulations.

1. Introduction

We treat an idealized problem that simultaneously models Langmuir circulations in the ocean and thermosolutal convection.

Langmuir circulations in the near-surface layers of natural bodies of water are convective motions thought to be driven by the action of the wind. These motions take a form approximated by a set of parallel lines on the surface known as windrows. The general distribution of density in the ocean, created by vertical variations of temperature and salt, lead to a density stratification that is generally stable, with density increasing with depth. Mixing caused by turbulence, surface cooling and

other agencies introduced at the air–water interface create a layer adjacent to the surface, the 'mixed layer', having properties that are nearly uniform with depth. Observations of downwelling motions associated with Langmuir circulations indicate sizeable vertical transport and suggest that the phenomenon is one of the significant mixing mechanisms acting in the mixed layer (Langmuir 1938; Weller *et al.* 1985; Thorpe 1985; Weller & Price 1988; see Leibovich 1983 for other references to observational data).

According to a theory proposed by Craik & Leibovich (1976), the vorticity deformation (of vorticity usually generated by the surface wind stress) caused by the particle drift in gravity waves can lead to motions of the Langmuir circulations (abbreviated henceforth as LC) type by inducing a mechanical instability (Craik 1977; Leibovich 1977*b*). The theory deals with an averaged set of equations in which only the rectified effects of the wave motion appear (in the form of the Stokes drift current). When the water column has a statically stable density stratification, the destabilizing tendencies caused by the wave–current interaction are resisted by the stabilizing action of buoyancy. Under these circumstances, the mathematical model describing such motions bears a close resemblance to the model usually used to describe thermosolutal convection in a system with unit Prandtl number (σ) heated from below and having solute concentration decreasing upwards. In fact, when the gradient of the Stokes drift engendered by the surface gravity waves is a constant and density variations arise from temperature variations only, the field equations governing Langmuir circulations and thermosolutal convection (with $\sigma = 1$) are identical (Leibovich 1983). The boundary conditions natural to the Langmuir circulation problem are different from those customarily applied to thermosolutal systems, although they are compatible with a physically reasonable thermosolutal problem.

In this paper, the dynamics of Langmuir circulations are explored with particular emphasis on circumstances having strong buoyancy effects. Under these conditions, stability is first lost to overstable motions. The mechanism leading to oscillations may be inferred by analogy with like behaviour in thermosolutal convection and other unstable systems of double-diffusive type. The essential mechanism was first identified by Stern (1960), and arises when the destabilizing agent (temperature in the thermohaline problem and momentum in the LC problem) diffuses more rapidly than the stabilizing agent (salt in the thermohaline problem and temperature in the LC problem considered here). Convection that fluctuates with time is expected to lead to weaker mixing effects, and so it is of particular interest to know whether the fluctuations appearing at the onset of convection persist when the system is further destabilized. Thus, the chief concern of this paper is the course taken by the system when conditions are not close to marginal and nonlinear effects dominate.

These issues are explored for a layer of water of finite depth and infinite horizontal extent, bounded above and below by an isothermal plane surface. A constant stress (due to wind) is assumed to be applied at the top boundary in a direction parallel to that of the Stokes drift of a statistically stationary and horizontally homogeneous set of surface gravity waves. A steady non-convective equilibrium solution to the LC problem exists with a unidirectional current in the direction of the applied surface stress and having constant stress through the water column. Two-dimensional perturbations of this system of roll form (invariant in the direction of the Stokes drift current) are examined which leave the temperature and stresses unchanged at the top and bottom boundaries. These boundary conditions model a stratified layer adjacent to the surface and bounded below by a deep thermocline with a much

stronger density gradient. So that we may establish as close a connection to double-diffusion problems as possible, we assume a constant Stokes drift gradient. The problem that we solve then may be interpreted also as a thermosolutal problem with salt concentration maintained at fixed (but differing) values at the horizontal plane boundaries, and constant vertical heat flux specified there (with $\sigma = 1$, and ratio of salt to heat diffusivity, τ, equal to 1/6.7, which is the inverse of a nominal molecular Prandtl number for water).

Moore *et al.* (1983) and Knobloch *et al.* (1986*b*, abbreviated henceforth as K) consider the nonlinear dynamics of the double-diffusion problem described in the previous paragraph for several values of σ and τ; but with constant temperature rather than constant heat flux prescribed on the bounding planes. This is a common choice for thermosolutal problems, since the linear dispersion relation is algebraic, and linear eigenfunctions may be found by inspection. We refer to this problem as 'ideal double-diffusion' (or IDD). Their work is intriguing since it shows the existence of period-doubling bifurcations in the solutions of the full partial differential equations governing a well-known problem in fluid mechanics. Furthermore, it indicates that a low-dimensional model, a system of five ordinary differential equations, provides a surprisingly faithful qualitative reproduction of a wide range of very complicated temporal behaviour found in fully resolved numerical solutions of the thermohaline problem. The five-mode set, originally derived by Veronis (1965) and explored in detail by da Costa, Knobloch & Weiss (1983), may be regarded as describing the time evolution of the coefficients of a minimal Galerkin truncation. The minimal truncation and the full system both reveal increasingly complex temporal behaviour for sufficiently large salt concentration gradient (the stabilizing agent, measured by a Rayleigh number S) as the destabilizing driving force (temperature difference, measured by a Rayleigh number, R) is increased. Depending on S, the possibilities include periodic time dependence, period-doubling bifurcations, period-doubling cascades to chaotic motion, and period-halving bifurcations. All of these possibilities lead, for sufficiently large R, to steady convection. A number of these features had been reported earlier by Huppert & Moore (1976). What is particularly surprising is the qualitative agreement between the dynamics of the minimal truncation and that of the full system, since in other fluid-mechanical systems (see, for example, Curry *et al.* 1984, or Marcus 1981) it is by now well established that the dynamics of low-order truncations is typically incorrect in most essential respects except near onset.

Given the similarity between this problem and our own, the findings of Moore *et al.* (1983) and K encouraged us to hope that a correspondingly simple model already explored by Leibovich (1985), Moroz & Leibovich (1985), and Moroz (1985) would capture the essential behaviour of the Langmuir circulation problem far from equilibrium. This turned out not to be the case. Although our five-mode truncation predicts bifurcation sequences similar to that of K, including period-doubling cascades to chaotic states, our fully resolved solutions with periodic sidewall boundary conditions show no period-doubling bifurcations or chaotic motion. The only time-dependent asymptotic states found are single-frequency periodic motions arising from the Hopf bifurcation. These periodic motions may exist in the form of either standing or travelling waves (or both forms coexisting). Standing waves alone are found for values of S at which the Hopf bifurcation is supercritical. At somewhat larger values of S, the Hopf bifurcation is to travelling waves and is found to be subcritical. Based upon general considerations (apparently first derived by Shechter 1976, see also Golubitsky & Stewart 1985) neither travelling waves nor standing

waves may then be stable for very small amplitudes. The travelling wave solutions emanating subcritically from the Hopf bifurcation appear to stabilize through a turning point and lead to robust finite-amplitude travelling waves. When both the travelling and standing waves branch subcritically, there is the possibility that both forms of solution, unstable for very small amplitudes based on Shechter's work, may each stabilize through turning points and lead to coexisting, stable, finite-amplitude solutions. We have found an example of this.

If the symmetries imposed in the works on IDD cited above, which require the lateral cell boundaries to be vertical, stress- and flux-free, are enforced, then we still find that the five-mode truncation fails to predict the observed course of events. We explore the effects of requiring this symmetry in the LC problem. We find no period doubling in this case, and less robust chaotic behaviour, but we do find regions of temporally complex dynamics. This includes, in addition to periodic motion with a period increasing smoothly with R, quasi-periodic motion with two incommensurate frequencies, two-period frequency-locked motion, chaos which succeeds a two-period frequency-locked state, and steady convective motion. The chaotic solutions appear to arise by the intermittent 'scenario' that has been described by Pomeau & Manneville (1980): here a periodic orbit is irregularly interrupted for irregular periods of time by aperiodic motion, with the periodic motion reforming in between the periods of bursts of aperiodic behaviour. In addition to losing complex temporal behaviour, the steady states found under constrained boundary conditions are found to lose stability to different steady states, or to nonlinear travelling or standing waves, when this symmetry is not imposed.

The doubly-periodic flows which arise in our LC and non-ideal double-diffusion (we use LC to refer to either) problems stem from degenerate points in parameter space where the flow is simultaneously marginally unstable to perturbations with two different wavenumbers and distinct frequencies. This possibility does not arise in IDD problems previously considered in the literature (with the exception of Nield 1967, who considered the linearized double-diffusive stability for a wide range of boundary conditions).

Some of the consequences of relaxing lateral boundary conditions in the ideal thermosolutal problem have recently been considered by Knobloch *et al.* (1986*a*). They find that the periodic oscillations ensuing from the Hopf bifurcation under constrained boundary conditions are unstable to travelling waves when general periodic conditions are imposed. Furthermore, they show the possibility of a degenerate Hopf bifurcation in the ideal thermosolutal problem under these lateral boundary conditions. Knobloch (1986) shows that, in the neighbourhood of this isolated point in parameter space, quasi-periodic motion with two and three independent frequencies can develop from interactions between travelling waves and standing waves, all with the same wavenumber, by successive bifurcations. This picture resembles one that we find here under constrained lateral boundary conditions, but in our case it arises from interactions between modes having distinct wavenumbers, as well as distinct frequencies.

It appears that spatially constrained configurations may give rise to flows of considerable temporal complexity: when spatial constraints are released, the system may trade temporal complexity for an increase, albeit a mild one, in spatial complexity. The powerful effects of stringent constraints have already been alluded to by Moore *et al.* (1983) and by K.

There are a number of reports indicating that the windrows (presumed to be) associated with Langmuir circulations sometimes drift at right angles to the wind

direction (see, for example, Van Straaten 1950; Meyer 1969; Thorpe & Hall 1982, 1983.) The simplest cause for such a drift is a large-scale surface current having a component normal to the wind direction. The drift observations by Thorpe & Hall seem to be due to such a current. The travelling waves found here offer another possible explanation, and one that should be easy to distinguish observationally.

Section 2 gives equations for Langmuir circulations, and describes the problems we wish to model. Linear stability characteristics relevant to this paper are also given in this section. Simpler models obtained for the LC problem by truncations of Galerkin expansions are discussed briefly in §3. These comprise truncations to five Galerkin modes, leading to dynamics with period-doubling cascades resembling those found by da Costa *et al.* (1983), as well as truncations to twenty and to thirty-eight modes. By the nature of their construction, these low-dimensional models have the potential to represent the dynamics only when the motion is subjected to constrained boundary conditions. Even then, only a limited number of qualitative features of these simplified models can be related to the solutions of the partial differential equations. The low-order truncations tend to yield period doubling not produced by the partial differential equations. As the number of terms, M, included in the truncation is increased, however, period doubling is deferred to larger values of S; in this sense the truncations improve as M is increased.

We present numerical results for motions subject to periodic boundary conditions in §4, constrained boundary conditions in §5 and conclusions are placed in §6.

2. Problem statement and linearized stability

We formulate our Langmuir circulation problem in this section, followed by a survey of the results of the linear stability analysis that are needed in this paper. More complete stability results for the LC problem may be found in Lele (1985). Corresponding information for the ideal thermosolutal problem may be found in Baines & Gill (1969); thermosolutal convection with other boundary conditions is treated in Nield (1967).

2.1. *Langmuir circulations in a layer of finite depth*

Craik & Leibovich (1976) assume the existence of gravity waves on the surface of a water body; the waves are assumed to be irrotational and to have fixed and prescribed characteristics. Rotational currents, usually taken to be generated by a fixed surface wind stress applied in the direction of wave propagation, are assumed to be weak compared with typical particle speeds of the wave motions. Wind-generated motion generally approximates to these assumptions. (Langmuir circulations may be supported by currents generated in other ways, provided waves are present. An interesting example is due to Craik (1984) who showed that circulations can exist in the absence of wind, with the current needed being the second-order Eulerian mean flows created by slow viscous decay of a surface wave field.) If a representation embodying these assumptions is substituted into the Navier–Stokes equation and followed by averaging to eliminate wave-induced fluctuations, equations for the mean motion are produced which form the basis for a theory of Langmuir circulations. Buoyancy effects due to temperature variations can be incorporated (Leibovich 1977*b*), using a Boussinesq approximation, and this extended set is adopted for the present study. This set is the ordinary Boussinesq approximation, with an additional apparent force due to the interaction of the waves and mean-flow currents; this force, expressed per unit mass, as $\boldsymbol{u}_s \times \boldsymbol{\omega}$ (Craik &

Leibovich 1976; Leibovich 1977*a*), where $\boldsymbol{u}_s$ is the (vector-valued) Stokes drift of the water waves, and $\boldsymbol{\omega}$ is the vorticity of the mean current. Here 'mean' refers to an average over timescales comparable with a period of the water waves; this focuses on motions, time-dependent in general, which evolve on timescales long compared with the characteristic period of the waves.

We consider a layer of water of depth d and infinite horizontal extent. The layer is bounded above by a free surface on which water waves with fixed, horizontally homogeneous characteristics (in a statistical sense) propagate, generating a Stokes drift in the x-direction; this drift will, by virtue of the assumptions concerning the wave field, depend on depth only. We take the plane $z = 0$ to be the mean free surface, and the lower boundary of the layer is taken to be the plane $z = -d$. A constant stress, ρu_*^2, is assumed to be applied (by the wind) in the x-direction across the plane $z = 0$, and the temperature of the water is held at a constant level $T = 0$ there; and it is assumed that the lower plane is maintained at a cooler temperature, $T = T(0) - \Delta T$.

A possible equilibrium solution to the governing equations is the conductive temperature distribution

$$T(z) = T(0) + (\Delta T/d)\, z,$$

leading to a linear (stable) density stratification, and a rectilinear constant stress (Couette) flow in the x-direction, with speed

$$U(z) = (u_*^2/\nu_T)\, z + U_0.$$

Here ν_T is the kinematic (eddy) viscosity of the water, assumed constant. If the plane $z = -d$ were a no-slip rigid wall, then $U_0 = (u_*^2/\nu_T)\, d$. This is appropriate for laboratory experiments in wind-wave tanks, but we wish to consider a model in which the constant momentum flux continues to be maintained through the layer, but in which the speed at the lower boundary is not directly controlled. We have in mind that our layer overlies a much deeper and heavier water body. The density difference is supposed to be so large that vertical motions of the interface may be ignored. The momentum flux through the upper layer is transmitted through to the underlying fluid, but we suppose that perturbations to this stress at $z = -d$, caused by any non-rectilinear perturbations which may exist in the upper layer, may be neglected. Thus perturbations to the basic state are considered stress-free at both upper and lower boundaries. Note that stresses are not related to the Stokes-drift gradient, and that this may have a non-zero gradient at $z = -d$. The presence of a density interface introduces the possibility of internal waves, but these are not considered here. Since surface gravity waves and internal waves decouple (Lamb 1932) to lowest order when the lower layer is of great depth compared with the upper layer, they may be considered independently, and the presence of a density interface on the surface waves may be neglected.

We assume that variations in the x-direction are ignorable, and introduce a stream function ψ to account for the velocity components, v and w, in the (y, z)-plane. Dimensionless variables for the perturbed system are adopted as follows, where the asterisk identifies dimensionless quantities:

$$(y, z) = d(y^*, z^*), \quad t = \frac{d^2 t^*}{\nu_T}, \quad u = U(z) + \frac{u_*^2\, d}{\nu_T} u^*(y^*, z^*, t^*),$$

$$\psi = \nu_T \psi^*(y^*, z^*, t^*), \quad v = \frac{\partial \psi}{\partial z} = \frac{\nu_T}{d} v^*, \quad w = -\frac{\partial \psi}{\partial y} = \frac{\nu_T}{d} w^*.$$

When substituted into the equations in Leibovich (1977*a*) this scaling leads to the following dimensionless equations (see also Leibovich 1983):

$$\left(\frac{\partial}{\partial t^*}-\nabla^{*2}\right)\nabla^{*2}\psi^* = Rh^*(z^*)\frac{\partial u^*}{\partial y^*}-S\frac{\partial \theta^*}{\partial y^*}+\mathrm{J}(\psi^*,\nabla^2\psi^*),$$

$$\left(\frac{\partial}{\partial t^*}-\nabla^{*2}\right)u^* = \frac{\partial \psi^*}{\partial y^*}+\mathrm{J}^*(\psi^*,u^*),$$

$$\left(\frac{\partial}{\partial t^*}-\tau\nabla^{*2}\right)\theta^* = \frac{\partial \psi^*}{\partial y^*}+\mathrm{J}^*(\psi^*,\theta^*),$$

where ∇^{*2} is the Laplacian and J* the Jacobian with respect to (y^*, z^*),

$$\mathrm{J}^*(f,g) = \frac{\partial f}{\partial y^*}\frac{\partial g}{\partial z^*}-\frac{\partial f}{\partial z^*}\frac{\partial g}{\partial y^*};$$

and

$$R = \frac{u_*^2 d^4}{\nu_T^3}\frac{\partial u_s}{\partial z}(0),\quad S = \frac{\beta g \Delta T d^3}{\nu_T^2},\quad \tau = \frac{\alpha_T}{\nu_T}, \tag{1}$$

where β is the coefficient of thermal expansion, g is the acceleration due to gravity, and α_T is the (eddy) diffusivity of heat, and we have written the Stokes-drift gradient as

$$\frac{\partial u_s}{\partial z}(z) = \frac{\partial u_s}{\partial z}(0)\,h^*(z^*),$$

so that $h^*(z^*)$ is its dimensionless form. This set is identical to that governing two-dimensional thermosolutal convection (with Prandtl number $\sigma = 1$) if $h^*(z^*)$ is set to unity. The parameters R and S are identified with the thermal and solute Rayleigh numbers in the thermosolutal problem, and τ, which in the LC problem is the inverse Prandtl number, is identified with the ratio of solute to heat diffusivities: furthermore, temperature perturbations θ^* correspond to solute concentration, and the x-momentum perturbation u^* corresponds to temperature perturbation in the thermosolutal problem.

We now drop all asterisks and consider only dimensionless variables. We also set $h(z) \equiv 1$, thus specializing the LC problem in such a way as to associate it with a thermosolutal problem. The approximation of constant Stokes-drift gradient implies a layer depth d small compared with a representative wavelength of the surface wave field. Thus the equations to be considered in this paper are

$$\left(\frac{\partial}{\partial t}-\nabla^2\right)\nabla^2\psi = R\frac{\partial u}{\partial y}-S\frac{\partial \theta}{\partial y}+\mathrm{J}(\psi,\nabla^2\psi), \tag{2a}$$

$$\left(\frac{\partial}{\partial t}-\nabla^2\right)u = \frac{\partial \psi}{\partial y}+\mathrm{J}(\psi,u), \tag{2b}$$

$$\left(\frac{\partial}{\partial t}-\tau\nabla^2\right)\theta = \frac{\partial \psi}{\partial y}+\mathrm{J}(\psi,\theta). \tag{2c}$$

Boundary conditions at the top and bottom of layers, consistent with the model LC problem posed, are

$$\psi = \frac{\partial^2\psi}{\partial z^2} = \theta = \frac{\partial u}{\partial z} = 0 \quad \text{at } z = 0, -1. \tag{3}$$

These correspond to a thermosolutal problem with stress-free boundaries, constant solute concentration and constant heat flux at the boundaries. Lateral boundaries are taken to be at $y = 0$ and $y = L$ and two forms are used:

$$(A) \qquad \psi = \frac{\partial^2 \psi}{\partial y^2} = \frac{\partial u}{\partial y} = \frac{\partial \theta}{\partial y} = 0 \quad \text{at } y = 0, L, \tag{4}$$

$$(B) \qquad \psi(0,z) = \psi(L,z), \quad u(0,z) = u(L,z), \quad \theta(0,z) = \theta(L,z). \tag{5}$$

Conditions (A), corresponding to vertical zero-flux boundaries, are a special case of conditions (B), which merely require periodicity of the flow with period L. We refer to (A) as 'constrained' and (B) as 'unconstrained'.

2.2. *Summary of linear stability for Langmuir circulation and for non-ideal double diffusion*

Stability of normal modes in this problem must be determined by solution of an eighth-order ordinary differential system, leading to a transcendental characteristic equation. The problem was treated by solving the differential system directly by a Galerkin method using basis functions constructed from Chebyshev polynomials: details of the numerical method, together with convergence and accuracy tests, are given in Lele (1985), where results for variable Stokes-drift gradient and in layers bounded below by a rigid no-slip surface may also be found.

The LC stability problem with boundary conditions (3) has,for all values of S, zero critical wavenumber. The critical value of R is 120.0. These results had previously been found by Nield (1967). Although the limit as the wavenumber $k \to 0$ corresponds to the critical conditions, the limit $k = 0$ corresponds to an infinitesimal disturbance with no vertical motion. To realize vertical motions, a non-zero wavenumber is required. We are thus led to suppose that some agency (lateral boundaries, or a limited lateral extent of an imposed surface wave or surface stress field) exists that serves to quantize the wavelengths that can be realized by the system. With a lateral extent of L, only the wavenumber $k = 2\pi/L$ and its harmonics, with wavenumbers that are integer multiples of the wavenumber of the fundamental, can be fitted into the domain. The 'cell' or 'roll' aspect ratio (ratio of lateral cell dimension to its height) is $q^{-1} = \frac{1}{2}L$, and it is convenient to work with $q(=k/\pi)$ rather than L. For $q = 1$, the cells are square, $q < 1$ corresponds to wide cells, $q > 1$ to narrow ones.

We deal only with values of $\tau = (6.7)^{-1}$, corresponding to a nominal molecular Prandtl number of 6.7 for water. Fixing first q, then S, we calculate the critical value R_c of R. For values of $q < 0.4$, onset of instability is to monotonic disturbances. Searches are made for a range of S up to 500 or greater in all cases. As q increases, overstable modes arise for the larger values of S in the search range, with the switchover occurring at $S = S^D(q)$: $S^D(q)$ decreases with increasing q, and at $q = 1$, $S^D \approx 78$. At S^D, the frequency of the marginal overstable modes vanishes. The variation of S^D with q may be inferred from figure 1, in which R_c is plotted against q for several values of S. The branch with onset to monotonic convection is labelled M, that for overstable motion is labelled H. Notice that, at least for the range of S shown, the minimum critical R for overstable motion occurs in a range of q between 0.75 and 1.

For a fixed value of q, the dependence of R_c on S is represented, to a good approximation, by a pair of straight lines as in ideal double diffusion. The ideal problem, however, is exactly represented by a pair of lines; as q varies, each member of this pair remains parallel. Motion in a periodic domain characterized by a value

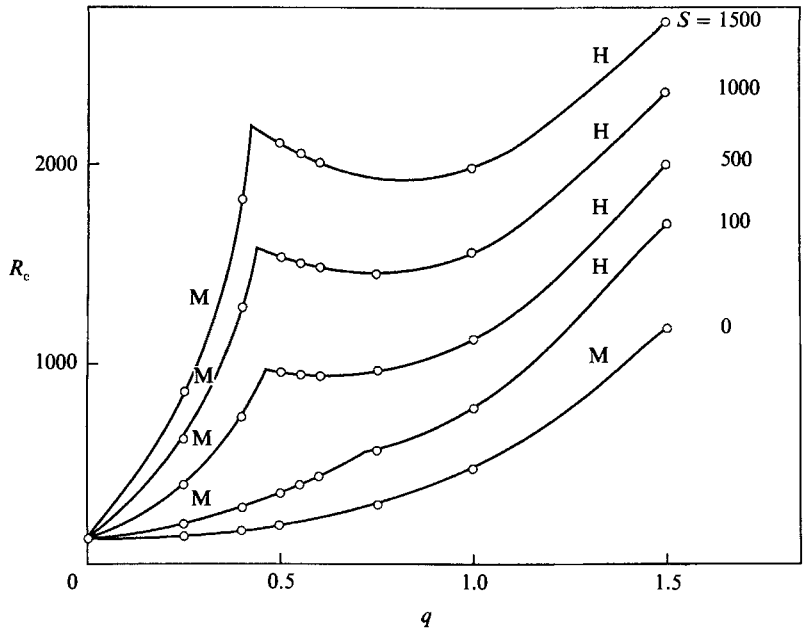

FIGURE 1. Variation of onset conditions with q (wavenumber/π) for various values of S. Portions of curves labelled M lead to monotonic convection, those labelled H to overstable convection. The value of S^{D} for a given q may be estimated from this figure.

of $q = q_1$, admits disturbances with $q = nq_1$ for any integer $n \geqslant 1$. Thus the system may be unstable to harmonics of the fundamental wavenumber, and the possibility exists that multiple bifurcations can exist at points where the fundamental and one of its harmonics, or two distinct harmonics of the fundamental, with distinct eigenfunctions and frequencies, are simultaneously marginally unstable. That this does happen is shown in figure 2, on which the transition curves in the (S, R)-plane are plotted for $q = 0.5n$, $n = 1, 2, 3$. In this figure, the lines labelled Mn, with $n = 1$, 2, or 3, represent the transitions to monotonic convection for modes with $n = 1$, 2, or 3, and the lines Hn, $n = 1$, 2, or 3, correspond to transition to overstable convection via a Hopf bifurcation for modes $n = 1$, 2, or 3. For purposes of reference, the straight-line data fit for H1 is given by $R^{\mathrm{H}} = 1.15S + 368$, the fit for H2 is $R^{\mathrm{H}} = 0.85S + 692$, and that for H3 is (approximately) $R^{\mathrm{H}} = 0.73S + 1624$. The monotonic convection limit M1 is fitted by $R^{\mathrm{M}} = 1.62S + 183$, M2 is fitted by $R^{\mathrm{M}} = 3.93S + 459$, and M3 by $R^{\mathrm{M}} = 5.26S + 1174$.

For a given mode n, the lines M and H intersect at some point, where a multiple bifurcation occurs: this point, S_n^{D}, separates the plane into two regions, $S < S_n^{\mathrm{D}}$, where the basic state loses stability to monotonic convection, and $S > S_n^{\mathrm{D}}$, where it loses stability to convection periodic in time. Thus, for the fundamental wavenumber, $n = 1$, $S_1^{\mathrm{D}} = 394$. Since the lines Mn, for $n > 1$, lie above M1, transitions to monotonic convection in this system always occur for mode 1, so that monotonic convection is possible for $S < 394$. At $S = 1080$, the Hopf lines H1 and H2 intersect, with H1 lying below H2 for $S < 1080$ and above for $S > 1080$. Thus, for $394 < S < 1080$, the system loses stability to time-periodic convection corresponding to the fundamental wavenumber, mode $n = 1$, but for a range of S exceeding 1080, it first loses stability to time-periodic convection with twice the wavenumber. The Hopf lines H3, H2

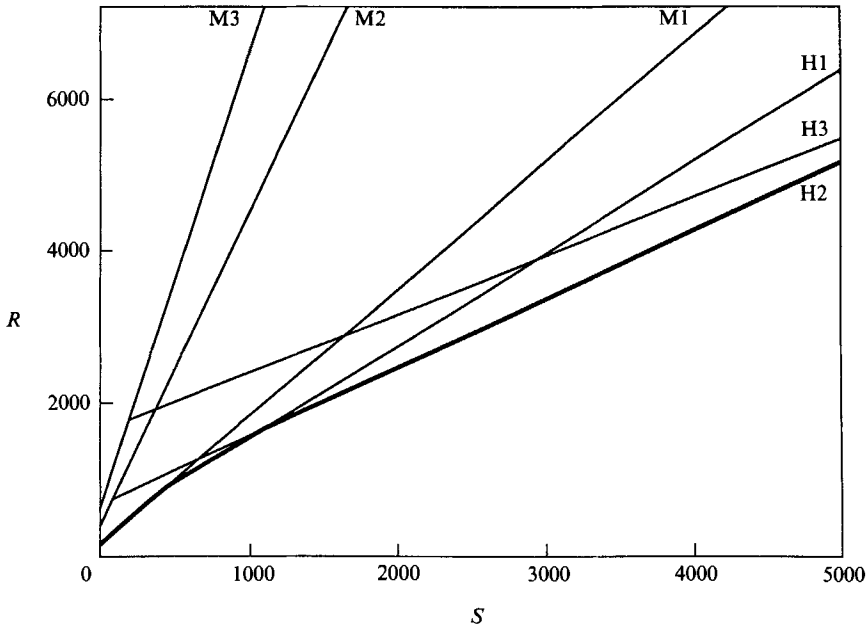

FIGURE 2. Linear stability for Langmuir circulations illustrating the possibility of multiple instabilities. Lines labelled Mn, with $n = 1$, 2, or 3 represent transitions to monotonic convection for modes having $q = n/2$. The lines Hn, $n = 1$, 2, 3 represent transitions to overstable motions via Hopf bifurcations. At intersection points, multiple instabilities are possible.

intersect (off the graph) at around $S = 7340$, so that mode 3 succeeds mode 2 as linearly most unstable mode at this point. Thus, the stability diagram is made up of a series of (nearly) straight-line segments, drawn with a heavy line in the figure. At each corner of the heavy line, multiple instabilities arise. Although the corner at S_1^{D} corresponds to zero frequency when approached either from above in S (through overstable conditions) or from below (monotonic conditions), the remaining corners correspond to two distinct frequencies. Thus, at the intersection of H1 and H2, for example, the frequencies differ by a factor of about 4.

The nonlinear evolution of unstable modes will be traced in remaining sections of this paper, and the interaction of modes with two different wavenumbers will have important consequences.

2.3. *Global measures of the disturbances*

We have elected to characterize the results of numerical computations of the nonlinear system evolution to be presented in subsequent sections of this paper by either local variables (such as the value of ψ at a particular grid point as a function of time) or by global variables such as net heat flux across the surface $z = 0$ or kinetic energy of the convective motion. Of these global measures, we find a dimensionless measure of the surface heat flux, the Nusselt number,

$$N_\theta(t) = 1 + \left\langle \frac{\partial \theta}{\partial z}(y, 0, t) \right\rangle \tag{6}$$

to be convenient in the LC problem. The angle brackets $\langle f \rangle$ here imply the horizontal average

$$\langle f \rangle = \frac{1}{L}\int_0^L f \,\mathrm{d}y.$$

In the non-ideal thermosolutal problem, this corresponds to the salt flux at $z = 0$.

Since $\partial u/\partial z$ vanishes at the boundaries, we do not have an analogue of a Nusselt number for the u-variable. Instead, we used a scaled value of the horizontally averaged surface momentum perturbation

$$\mathscr{M}(t) = K\langle u(y, 0, t)\rangle, \tag{7}$$

and take $K = 2/\Delta z$, where Δz is a z-mesh spacing in the numerical method, as a convenient scaling factor.

3. The truncated systems

We can compare the behaviour associated with the partial differential equations for the constrained LC problem to that associated with low-order systems of ordinary differential equations by writing

$$\left.\begin{aligned}
\psi(y,z,t) &= \sum_{m=1}^{\infty}\sum_{n=1}^{\infty} a_{mn}(t)\sin mq\pi y \sin n\pi z,\\
u(y,z,t) &= \sum_{m=0}^{\infty}\sum_{n=0}^{\infty} b_{mn}(t)\cos mq\pi y \cos n\pi z,\\
\theta(y,z,t) &= \sum_{m=0}^{\infty}\sum_{n=1}^{\infty} d_{mn}(t)\cos mq\pi y \cos n\pi z,
\end{aligned}\right\} \tag{8}$$

and substituting into (2) to obtain an infinite system of equations for the time-varying coefficients $a_{mn}(t)$, $b_{mn}(t)$ and $d_{mn}(t)$. These expansions satisfy the relevant boundary conditions, and thus constitute one possible Galerkin projection. We shall concentrate on three truncations of this system, involving 5, 20 and 38 modes.

The lowest-order non-trivial truncation (meaning one permitting nonlinear effects to distort the horizontal averages of u and θ) is obtained by retaining one mode only in the expansion for ψ: $a_{11}(t)$; and two modes each in the expansions for u: $b_{10}(t)$, $b_{01}(t)$, and for θ: $d_{11}(t)$, $d_{02}(t)$. If we relabel $[a_{11}(t), b_{10}(t), b_{01}(t), d_{11}(t), d_{02}(t)]$ by

$$\left[\frac{2\sqrt{2}}{q}(1+q^2)^{\frac{1}{2}}a(t^*), \frac{-2\sqrt{2}}{\pi(1+q^2)^{\frac{1}{2}}}b(t^*), \frac{-c(t^*)}{\pi}, \frac{2\sqrt{2}}{\pi(1+q^2)^{\frac{1}{2}}}d(t^*), \frac{e(t^*)}{\pi}\right],$$

where $t = t^*/\pi^2(1+q^2)$, and introduce

$$\left(\frac{8}{\pi}R, S\right) = \frac{\pi^4}{q^2}(1+q^2)^3(t, s), \quad \omega = \frac{4}{1+q^2}, \quad \gamma = \frac{q^2}{1+q^2},$$

then we obtain the set of equations:

$$\left.\begin{aligned}
\dot{a} &= -a + rb - sd, \quad \dot{b} = -\gamma b + a\left[\frac{2}{\pi} - \frac{c}{2}\right], \quad \dot{c} = \omega\left[-\frac{c}{4} + ab\right],\\
\dot{d} &= -\tau d + a[1-e], \quad \dot{e} = \omega[-\tau e + ad]
\end{aligned}\right\} \tag{9}$$

which was originally derived by Leibovich (1985) and analysed by Moroz & Leibovich (1985, referred to hereafter as ML).

n	$\mathbf{M}_n$	$\mathbf{H}_n$	R_n^{D}	S_n^{D}
1	$R = 1.64S + 187.8$	$R = 1.18S + 377.8$	863.6	410.8
2	$R = 4.12S + 480.6$	$R = 0.94S + 718.6$	789.8	75.2
3	$R = 5.70S + 1269.4$	$R = 0.84S + 1776.0$	1863.4	104.3

TABLE 1. Stability boundaries for wavenumbers $q = 0.5n$ for $\tau = 0.15$, as given by the five-mode model. $\mathbf{M}_n$ denotes onset of monotonic convection, $\mathbf{H}_n$ denotes onset of oscillatory, overstable convection, $(R_n^{\mathrm{D}}, S_n^{\mathrm{D}})$ denote the intersection points of the $\mathbf{H}_n$ and $\mathbf{M}_n$ boundaries.

This system closely resembles (differing only in the values of the coefficients) a five-mode model for thermohaline convection with unit Prandtl number, originating with Veronis (1965) and more recently studied by da Costa *et al.* (1983).

There are a maximum of five possible equilibrium states, depending on the various parameters; they are obtained (ML) by substituting the real roots of the quintic

$$a\left\{\frac{r}{\pi(\frac{1}{2}\gamma + a^2)} - \frac{s\tau}{\tau^2 + a^2} - 1\right\} = 0$$

into the vector

$$(a, b, c, d, e) = \left(a, \frac{a}{\pi(\frac{1}{2}\gamma + a^2)}, \frac{4a^2}{\pi(\frac{1}{2}\gamma + a^2)}, \frac{a\tau}{\tau^2 + a^2}, \frac{a^2}{\tau^2 + a^2}\right).$$

Thus the rest state $(a, b, c, d, e) = (0, 0, 0, 0, 0)$ is always an equilibrium state, and the point symmetry $(a, b, c, d, e) \mapsto (-a, -b, c, -d, e)$ ensures that the remaining finite-amplitude states occur in pairs.

We can study the stability of the rest state by seeking solutions proportional to $\mathrm{e}^{\lambda t}$, where $\mathrm{Re}(\lambda) > 0$ indicates instability and $\mathrm{Re}(\lambda) < 0$ indicates stability. When $\lambda = 0$ monotonic convection obtains, while for $\lambda = \pm \mathrm{i}\omega$ overstable convection obtains. In addition a multiple bifurcation $\lambda = 0$ (twice) is possible where these two stability boundaries intersect. Table 1 shows the stability boundaries for monotonic ($\mathbf{M}_n$) and overstable ($\mathbf{H}_n$) convection for $\tau = 0.15$ as functions of $q = 0.5n$, for $n = 1, 2, 3$. Also shown are the points $(S_n^{\mathrm{D}}, R_n^{\mathrm{D}})$ of intersection of $\mathbf{H}_n$ with $\mathbf{M}_n$. The agreement between the linear stability characteristics of the five-mode system and the partial differential equations (see §2) is very good. Moreover, both predict zero critical wavenumber for the onset of steady convection.

A weakly nonlinear analysis in the neighbourhood of the multiple bifurcation point $(s^{\mathrm{D}}, r^{\mathrm{D}})$ results in a second-order amplitude equation for the evolution of $a(t)$, which we may write as (ML)

$$\dot{q} = p, \quad \dot{p} = \alpha q + \beta p + Mq^3 + \Gamma q^2 p, \tag{10}$$

where q is a rescaling of $a(t)$, α, β, M and Γ are functions of the various parameters (α, β also depend on r and s, the perturbations from r^{D} and s^{D}). For $q = 1$, $\tau = 0.15$ we find that $M > 0, \Gamma < 0$ and the behaviour associated with (10) is described in detail by ML, to which the reader is referred; we shall briefly summarize the main results here.

Between the stability boundaries for monotonic and overstable convection we find a line of heteroclinic bifurcations, denoting the parameter values for which the period of oscillation becomes infinite. Numerical integrations of (9) (Moroz 1985) show that sufficiently close to the point $(s^{\mathrm{D}}, r^{\mathrm{D}})$, the variation of the period with r is monotonic; only simple symmetric or asymmetric oscillations are possible. For larger values of

s period-doubling bifurcations can occur, leading ultimately to chaotic behaviour; the variation of period with r is now multivalued in character (Glendinning & Sparrow 1984). For $s < s_k$ the onset of finite-amplitude convection is via a supercritical pitchfork bifurcation, whereas for $s > s_k$ subcritical steady convection is possible; s_k is the value of s for which a saddle-node bifurcation of the steady states first appears. The Hopf bifurcation first appears for $s = s^D > s_k$, and for $s > s^D$ there is no unique region of oscillatory convection; if we fix s and increase r then subcritical steady convection always precedes the onset of oscillatory motion in contrast to behaviour predicted from the partial differential equations. Moreover, the five-mode system is capable of supporting large-amplitude oscillations which encircle all the equilibrium states. Such oscillations have not yet been observed in either thermohaline convection or in any of the other related models of double-diffusive convection. These large-amplitude oscillations are associated with the vanishing of M or Γ in (10) (Moroz 1986).

If we define a thermal Nusselt number

$$N_\theta(t) = 1 + \pi \sum_1^\infty n d_{0n}(t) \tag{11}$$

for the truncated models by analogy with (6), then (11) gives $N_\theta - 1 = 2e(t) \leqslant 2$. It will be apparent from the integration of the partial differential equations to be reported in succeeding sections that much larger Nusselt numbers are possible. This fundamental disagreement is due to the upper limit on vertical temperature gradients imposed by the truncation. A similar limitation of course is present in the thermohaline problem.

If we now include all modes up to $m = 3$, $n = 3$ in (8), together with the two modes $b_{04}(t)$, $d_{04}(t)$, then we obtain a set of 38 nonlinear coupled equations (from which the reader will be spared!). In order to test the robustness of the behaviour found in the five-mode system to the presence of these additional modes, we have repeated some of our original computations.

In all of the integrations 18 of the 38 modes decayed rapidly to zero (the same 18 in each case) leaving a 20-mode system which gave identical results to the 38-mode system. The linear stability characteristics agree well with those for the partial differential equations and it is now possible for the Hopf bifurcation to precede the onset of subcritical steady convection. This occurs for $s \geqslant 150$ (as compared to $S \geqslant 350$ for the partial differential equations).

Period-doubling bifurcations as well as aperiodic oscillations occur in both the 20- and 38-mode systems, but their appearance is delayed to larger values of s (the first observation of a period-2 orbit was for $s = 904$ with the 20-mode model, compared with $s = 350$ with the five-mode model). The maximum value of N_θ at the saddle node is more difficult to compute but appears to be 4. Finally, we were unable to locate the large-amplitude oscillation which occupies a substantial part of the five-mode parameter space discussed by Moroz (1986); and we conclude that this kind of motion is an artifact of the truncation.

4. Motion under periodic boundary conditions

Nonlinear evolution has been studied using a finite-difference numerical scheme described in detail in Lele (1985); its general features are summarized in the Appendix. When S exceeds S^D, stability is first lost to overstable motions by a Hopf bifurcation at $R = R^H$. With the general periodic boundary conditions considered in

this section, the Hopf bifurcation can produce oscillatory motions which can take one of two forms (Schechter 1976; Golubitsky & Stewart 1985); travelling waves (TW), which are oscillatory in the frame in which the basic state is specified, but are steady in some reference frame translating uniformly at right angles to the basic velocity vector; or standing waves (SW), which are oscillatory in all reference frames. Like steady states, the TW solutions are characterized by time-independent global quantities, such as Nusselt number. It can be shown (see Golubitsky & Stewart 1985) that only one of these two kinds of solution can be stable near R^{H}, and then only if both the TW and SW branches bifurcate supercritically. We find that for a limited range of S, $S^{\mathrm{D}} < S < S^{\mathrm{sub}}$, where S^{sub} is a value lying between 400 and 500, the Hopf bifurcation is supercritical, and the oscillatory motion at onset is in the form of a standing wave (SW). For a limited range of S beyond S^{sub} the TW is subcritical; SW are not found, but finite-amplitude TW's are realized. For one value of S beyond this range, we have found coexisting finite-amplitude TW and SW, consistent with both TW and SW branches bifurcating subcritically and having turning points.

The calculations presented in this section are for values of $q = 1$, corresponding to a computational domain of width $L = 2$. Other choices with L of this approximate size appear from sample calculations to yield similar results.

For $q = 1$, the linear stability data presented in §2 indicates that the stability boundary for monotonic convection is fitted (with an error of 0.05%), over the range of S that we consider, by the line in the (S, R)-plane

$$R^{\mathrm{M}} = 459 + 3.93S$$

and that for overstable convection (the Hopf bifurcation, error less than 1.5%) by

$$R^{\mathrm{H}} = 692 + 0.85S.$$

These intersect at $S = S^{\mathrm{D}} = 76$, $R = R^{\mathrm{D}} = 757$; for $S < S^{\mathrm{D}}$, the $R^{\mathrm{M}}(S)$ is the linear stability boundary, for $S > S^{\mathrm{D}}$, it is $R^{\mathrm{H}}(S)$.

Numerical traverses have been taken at $S = 0$, 50, 150, 350, 400, 450, 600, 1500 and 3000. In each case, R is increased until a limit cycle or steady convection results from a weak numerical perturbation. The solution branch is then traced as R is further varied (by either increasing it or decreasing it). This section describes computations made with general periodic lateral boundary conditions. The effects of replacing these by the more restrictive no-flux lateral conditions, which do not permit travelling waves, are assessed in the next section.

For $S < S^* < S^{\mathrm{D}}$, the bifurcation to steady convection is supercritical, while for $S > S^*$, the bifurcation is subcritical. We have not determined the precise value of S^*; at $S = 0$ the bifurcation is supercritical, for $S \geqslant 50$, it is subcritical. Bifurcation diagrams for $S = 0$, 50 and 150 are shown in figure 3, with R as bifurcation parameter and $N_\theta - 1$ as amplitude measure. The solid curves give the branches of nonlinear stable steady states. Our numerical simulations use time-dependent schemes, and are not capable of capturing the unstable branch of steady states (shown as dashed lines). Therefore, the locus of points on this branch is only a schematic illustration, although the end points are correctly shown in figure 3(*a*, *b*); in figure 3(*c*), the bifurcation point for steady circulations is too large to be shown on the scale of the figure, as it occurs at $R = 1048$. A Hopf bifurcation arises for $S > S^{\mathrm{D}} = 78.2$, and this bifurcation point is marked with an H in figure 3(*c*). As R is increased, the Hopf bifurcation is encountered first if $S > S^{\mathrm{D}}$, and the onset of instability is oscillatory with bifurcating solutions taking the form of either standing or travelling waves.

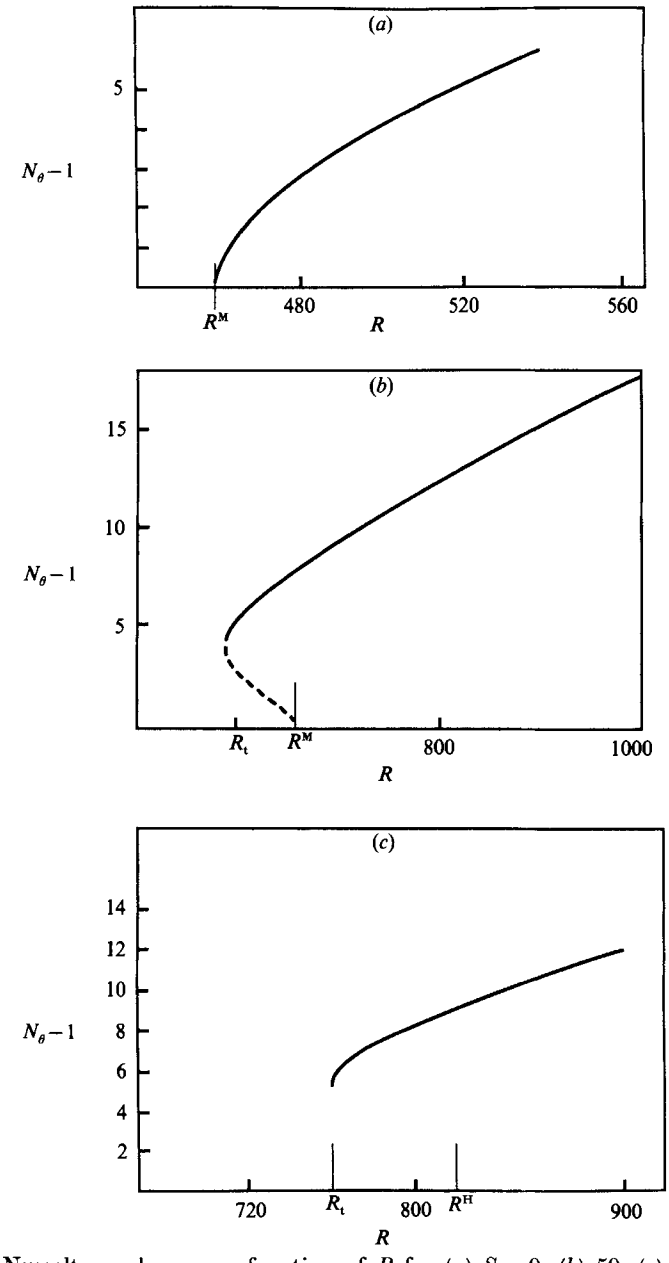

FIGURE 3. Nusselt numbers as a function of R for (*a*) $S = 0$, (*b*) 50, (*c*) 150. The solid curves represent stable steady convective motion under general periodic lateral boundary conditions. The dashed lines are schematic representations (not computed) of unstable steady states: these meet the stable branches at the turning points, labelled R_t. The Hopf onset is marked by an H, and the monotonic onset by an M. The latter is off the graph in (*c*).

The points labelled R_t in the figures are turning points, saddle-node bifurcations that divide the stable from the unstable branches of steady states.

Figure 4 (*a*, *b*) shows streamlines and vorticity contours for two points on the solid curve of figure 3 (*c*) ($S = 150$). Figure 4 (*a*), at $R = 760$, is close to the turning point R_t; figure 4 (*b*) corresponds to $R = 900$, the last point shown in figure 3 (*c*). For

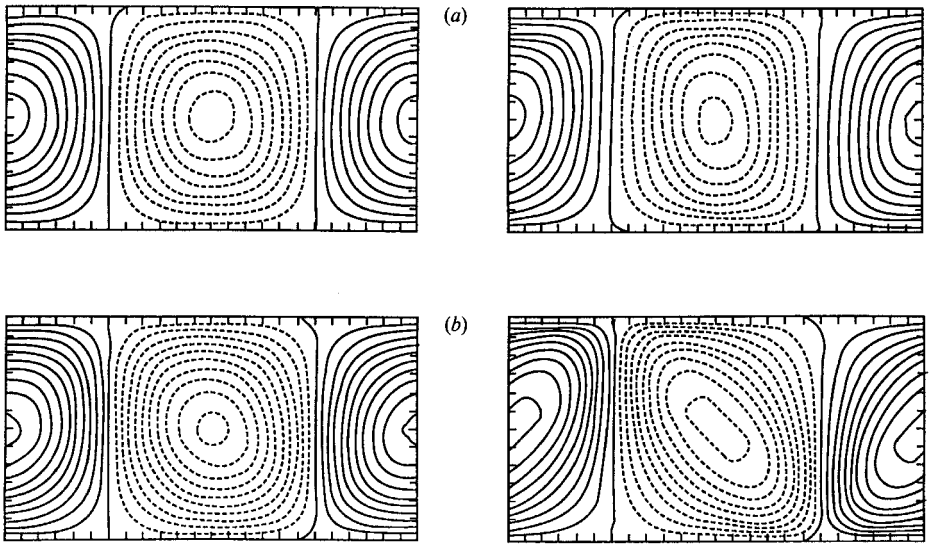

FIGURE 4. Streamlines (left figure) and vorticity contours (right figure) for $S = 150$. (*a*) $R = 760$, close to the turning point in figure 3(*c*). (*b*) $R = 900$, the last point in figure 3(*c*).

$R = 760$, the streamlines are almost symmetric about vertical lines passing through cell centres, while for $R = 900$, each streamline has rough symmetry about a line tilted from the vertical. This tilting is even more apparent in the vorticity contours.

The streamlines forming the cell boundaries for these flows are straight and vertical and these lateral boundaries are stress-free and have zero heat flux. These constraints are not imposed, but as the flow evolves, these conditions are maintained. This does not remain true for calculations at larger values of S.

At $S = 350$, cell boundaries no longer are straight and vertical or stress- and flux-free. The solid curve in figure 5 is a bifurcation diagram for this value of S, and gives Nusselt numbers of steady stable states. The turning point (and the unstable steady branch, not shown) has smaller Nusselt number, hence weaker disturbances, than does the corresponding point at smaller values of S. Thus, for R slightly greater than R_t, weaker finite-amplitude disturbances are required for transition to steady convection than is the case at smaller values of S.

The form of the motion is shown in figure 6 for two values of R. Figure 6(*a*) shows the streamlines and vorticity contours for $R = 965$, which is approximately at the turning point, and figure 6(*b*) is at $R = 1160$, which is the last point shown on the solid curve in figure 5. The cell sides now tilt and zero level curves of stream function and vorticity no longer coincide.

Whereas for $S = 150$ the two cells comprising the motion have mirror-image symmetry about the plane separating them, this is no longer true at $S = 350$. The symmetry can be imposed, however, by applying constrained boundary conditions rather than the general periodic ones. If these are applied at $y = 0$ and 2, then symmetry may or may not be enforced, because the boundary dividing the two cells is free to tilt (or to move). Nevertheless, we find that the symmetry is maintained with boundary conditions constrained in this way, at least for $S = 350$. (At larger S this is not so, and to find motions with straight and stress-free boundaries, we must allow only one cell in the computational domain by applying constrained conditions over half the lateral region, i.e. at $y = 0$ and $y = 1$.) We do not display the stream

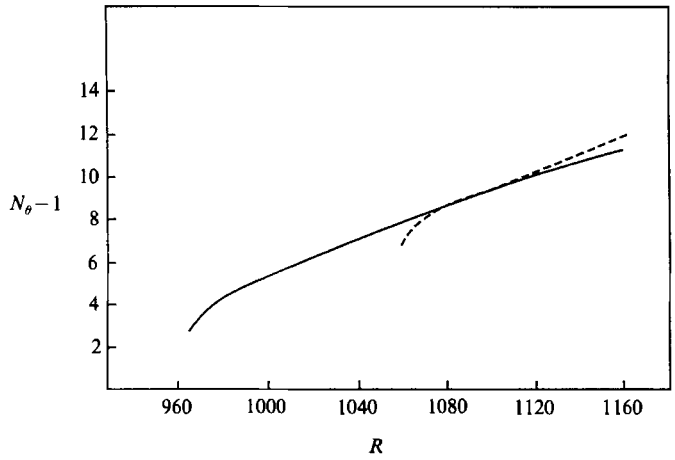

FIGURE 5. Nusselt numbers at $S = 350$ for stable steady states, shown as a function of R. The solid curve is obtained with general periodic boundary conditions and the dashed curve with constrained boundary conditions. The Hopf bifurcation occurs at approximately $R = 990$.

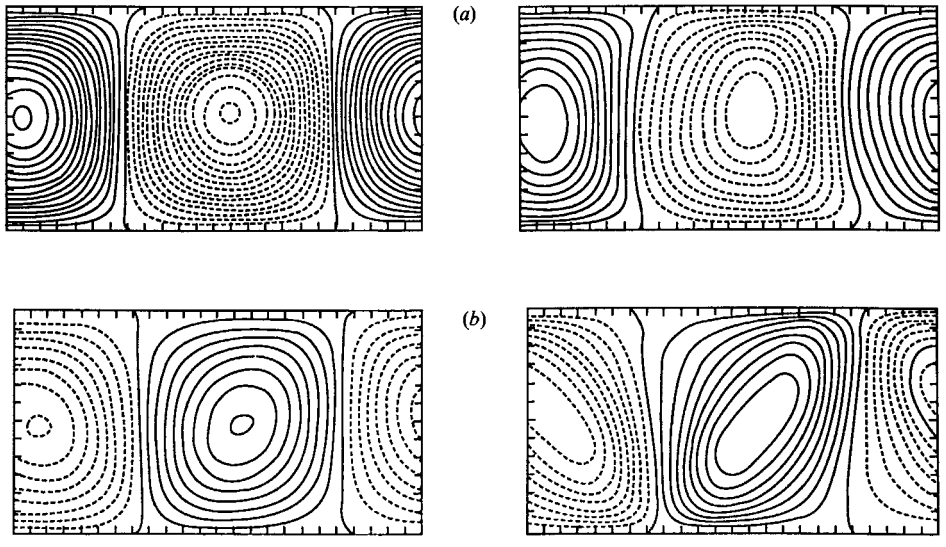

FIGURE 6. Streamlines and vorticity contours as in figure 4, but for $S = 350$. (*a*) $R = 965$, close to the turning point of the solid curve in figure 5. (*b*) $R = 1160$, the last point on the solid curve of figure 5.

function and vorticity contours of the constrained motions, since they closely resemble those of figure 4. The dashed line in figure 5 shows the stable steady states for $S = 350$ when the motion is subjected to the constrained boundary conditions. These steady states are *not* stable if the constrained boundary conditions are relaxed. We have tested their stability by computing first under the constrained conditions until steady solutions on the dashed curve are established, then adding a weak perturbation that breaks the symmetry, allowing the subsequent evolution under general periodic boundary conditions. In all cases, the system moves from steady states on the dashed curve to steady states on the solid curve. This statement remains true for all values of S larger than 350, although for all of the values of

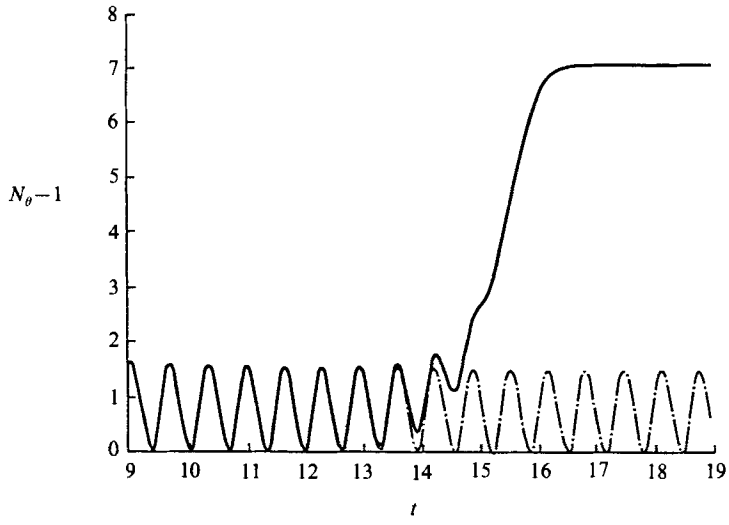

FIGURE 7. Time trace of shifted Nusselt number $N_\theta - 1$ for $S = 350$, $R = 1040$ and $q = 1$. The broken curve is computed with constrained flux-free vertical sidewall boundary conditions, and leads to oscillatory convection. The solid curve is computed using the oscillatory solution as initial data and periodic sidewall boundary conditions: it shows the oscillatory convection to be unstable to steady convection under periodic boundary conditions.

$S > 350$ that we have computed, the constrained steady states first lose stability to travelling waves rather than to steady states when the flux constraint is released. As R is increased further transitions to another branch of travelling waves, or to a steady solution branch may occur.

Notice that the turning point on the solid curve in figure 5 occurs at considerably smaller values of R than for the dashed curve, so that the region of subcritical steady convection is much deeper for the former case. It is also interesting to note that the constrained case has, for large enough R, larger heat transfer than the unconstrained case. Since the constrained states are unstable, the system clearly does not maximize heat transfer for the larger values of R.

For $S = 350$, a Hopf bifurcation to oscillatory convection in the form of standing waves occurs at $R = R^{\mathrm{H}}$. This is a supercritical bifurcation, a fact that we infer by observing that we do indeed compute time-periodic motions for R slightly exceeding R^{H}, but no non-trivial time-asymptotic states below it. The frequency of these marginally supercritical motions is close to the corresponding linearly unstable solution. The amplitude measures of the supercritical SW motions increase as R increases, and the frequency decreases.

These periodic SW states can be followed only for a small interval in R. Where they exist, they turn out to have vertical flux-free cell boundaries, and therefore are also solutions for the constrained case (A) in (4), although no constraint was imposed. This symmetry is lost simultaneously with the termination of periodic motion, and its replacement by steady convection, at a value of R only slightly above R^{H}. Thus, it appears that these periodic states are associated with motion having the spatial symmetry found in (A), and that they are unstable to a less symmetric steady state. The event sequence for $L = 2$ at $S = 350$ illustrates this behaviour. The onset of periodic convection occurs at $R^{\mathrm{H}} = 985.4$, with frequency of the oscillation being $\omega_{\mathrm{c}} = 5.826$ (period at onset is $T_{\mathrm{c}} = 2\pi/\omega_{\mathrm{c}} = 1.077$). As R increases, the period

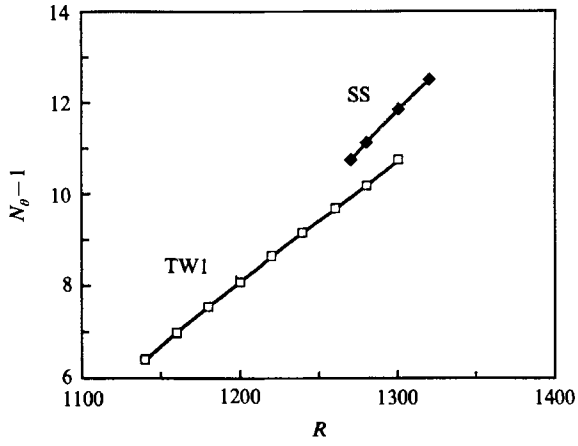

FIGURE 8. Shifted Nusselt number *vs.* R. for the overlapping travelling waves and steady-state solution branches found at $S = 450$.

increases, and at $R = 990, T = 1.12$, and the cell boundaries are, as they are at onset, vertical and stress- and flux-free. At $R = 1040$, the limit cycle is not found; instead, monotonic convection with cell boundaries that are no longer vertical and stress- and flux-free prevails. Apparently, the periodic motion loses stability and the system is attracted to a monotonic convective state at some $R = R^{\mathrm{HM}}(S)$, where $R^{\mathrm{HM}}(350) < 1040$. This loss of stability of the periodic motions, arising under mildly supercritical conditions (at $S = 350$, $(R^{\mathrm{HM}}(S) - R^{\mathrm{H}})/R^{\mathrm{H}} \leqslant 0.055$) may be seen in figure 7. This shows time series for $N_\theta - 1$ for two calculations. One is a periodic motion obtained by forcing vertical stress-free boundaries (as in the following subsection). The second is found using identical initial conditions, but with periodic boundary conditions: after tracing out the same path for a number of oscillation cycles, the system settles into a steady state.

We have attempted to trace steady states at larger S under general periodic boundary conditions. For $S = 450$, we found a stable steady state which we traced for a limited range of R between 1270 and 1320, and a stable travelling wave solution branch traced again for a limited range of R between 1140 and 1300. We presume that both of these branches may be continued further, but we have not done so. We shall refer to this family of travelling waves as 'TW1', to distinguish them from a second family found at larger S. Notice that the steady state and the TW1 branches coexist: it would be of interest to know whether these branches connect at some value of R, but we have not further explored the question. Figure 8 displays the shifted Nusselt number *vs.* R behaviour that has been found for these two solution branches. Figure 9(*a*) gives the variation of the travelling wave speed as a function of R for the TW1 branch, and figure 9(*b*) shows a progression of stream-function snapshops for the TW1 at $R = 1140$ (the first point on figure 8). The stream-function contour shape changes only slightly over the range of R shown in figure 8, and the steady-state stream function looks much the same. The situation at $S = 600$ (not shown) is similar to that at 450, only the motions are more vigorous, the distortion of cells and vorticity contours is more exaggerated, the Hopf bifurcation point occurs at $R = R^{\mathrm{H}}$, closer to the turning point value of $R = R_{\mathrm{t}}$. We did not calculate beyond $R = 1400$, and obtained only travelling waves.

All of the steady and travelling wave solutions found under general periodic

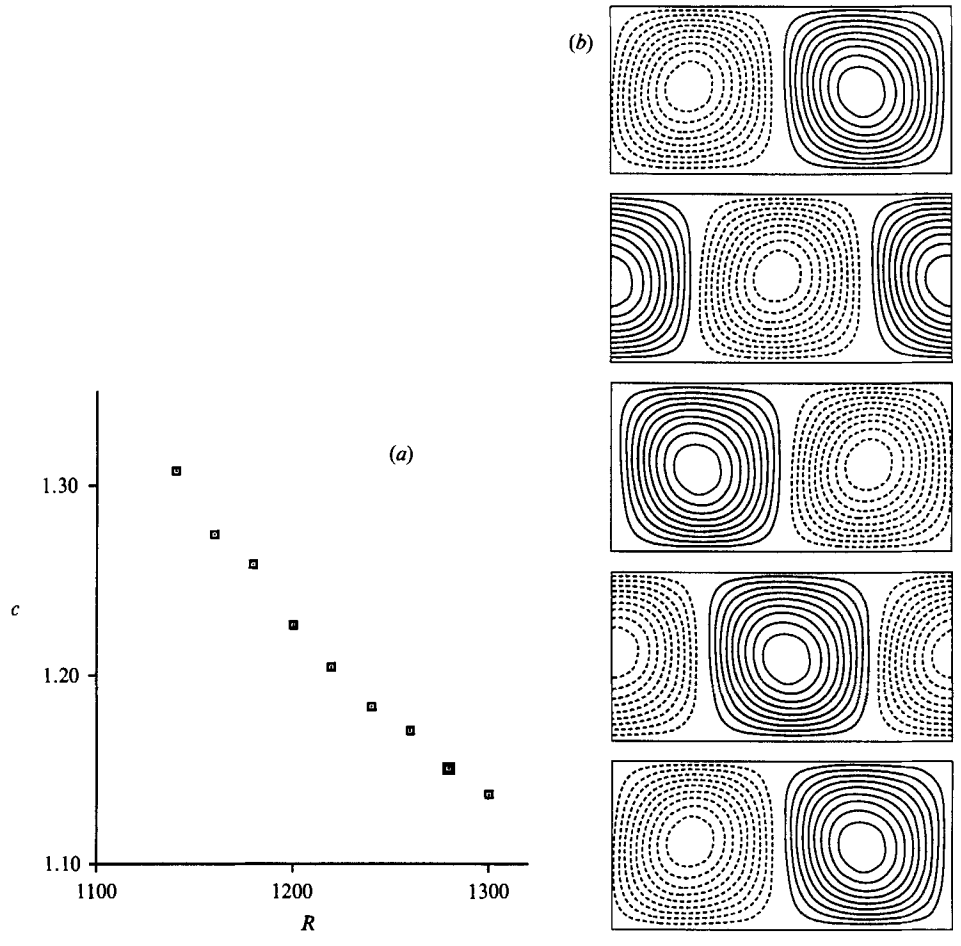

FIGURE 9. (*a*) Variation of the travelling wave speed as a function of R for the TW1 branch at $S = 450$. (*b*) Sequence of instantaneous stream function contours for the TW1 branch at $S = 450$, $R = 1140$.

boundary conditions exhibit a (flip) symmetry about the midplane permitted by the problem but not forced by the numerical method: $\psi(y, z, t) = -\psi(y+\frac{1}{2}L, -1-z, t)$, a symmetry shared by the streamwise velocity and temperature pertubations u and θ, and the vorticity. In addition, all of the steady-state and travelling wave solutions presented so far have 'staggered' cell centres, which lie alternately above and below the horizontal midplane, $z = -\frac{1}{2}$. It is easiest to see this, as well as the flip symmetry, in the vorticity contours.

For some value of S between 600 and 1500 another bifurcation takes place. The nature of this transition may be seen in the bifurcation diagram of figure 10(*a*, *b*) for $S = 1500$ and 3000. As R is reduced from large values, the curve is at first similar to that seen before, and we identify the travelling waves on this branch with TW1. Now, however, a break occurs in the curve at a point R^*, and it continues off at a different angle and seems to approach its termination with an infinite slope, consistent with a turning point. Figure 10(*c*) gives the speeds of these travelling waves. On the TW1 branch, the motion is qualitatively as before: cell centres are

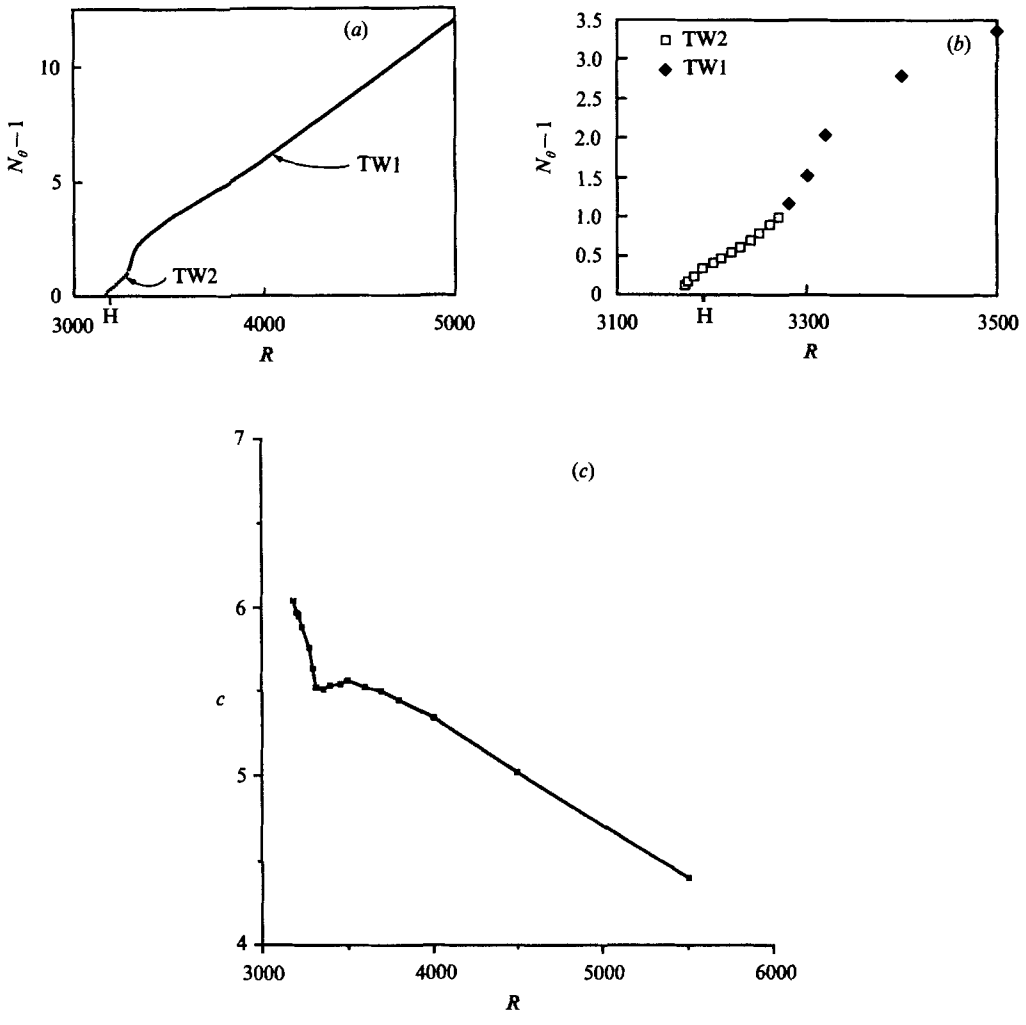

FIGURE 10. (*a*) Nusselt number *vs.* R for $q = 1$, showing a bifurcation between two branches of travelling waves, TW1 and TW2 for $S = 3000$. (*b*) Detail of part (*a*) to larger scale: the location of the Hopf bifurcation ($R = 3191$) is marked. (*c*) Variation of the travelling wave speed as a function of R for the travelling wave branches at $S = 3000$.

offset from the horizontal midplane. On the other hand, the new, lower R, branch has cells that continue to have curved boundaries and flip symmetry, but cell centres no longer have 'stagger'. Instead they are located, to the accuracy of the numerical scheme, precisely on the midplane, $z = -\frac{1}{2}$. This is determined by a detailed examination of the number fields generated for vorticity and stream function. Figure 11 shows vorticity contours at $S = 3000$, illustrating the bifurcation. The first two panels are on the TW2 branch, at $R = 3240$ and 3280, and the remaining two are at $R = 3360$, and 3400, are on the TW1 branch. The TW1 branch is replaced by the TW2 branch for R below the bifurcation value R^*.

Decreasing R on the TW2 branch below the values shown in figure 10 causes the computations to converge to the trivial non-convective states with an indication of the steepening associated with the turning point of a saddle-node bifurcation. Notice

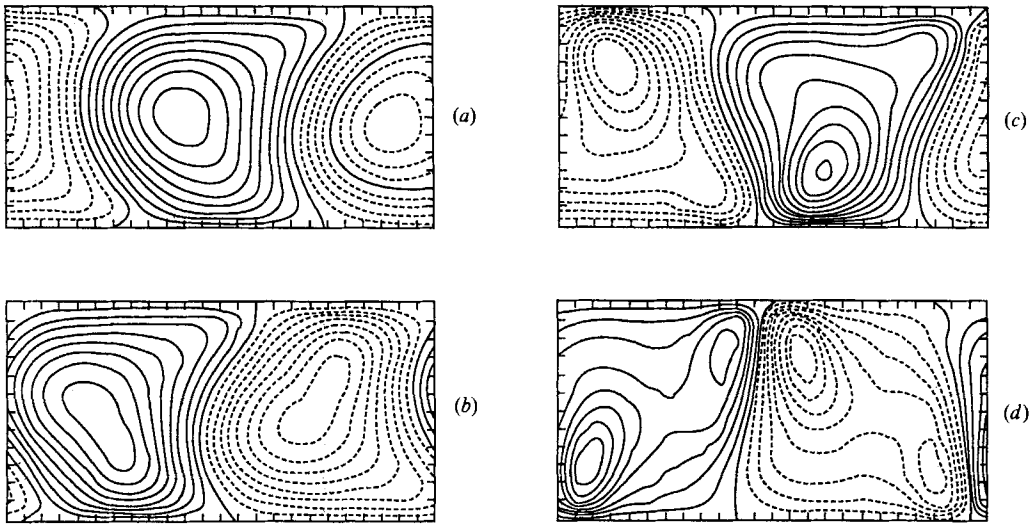

FIGURE 11. Vorticity contours at $S = 3000$. (a) $R = 3240$, (b) 3280, (c) 3360, (d) 3400. (a) and (b) are on the TW2 branch, (c) and (d) are on the TW1 branch.

that the smallest values of R for which TW2 solutions have been found are below the Hopf bifurcation points (e.g. at $S = 3000$, the Hopf bifurcation occurs at $R = 3191$, and the apparent turning point for TW2 solutions is just below $R = 3172$); thus the Hopf bifurcation to travelling waves is subcritical

We have also found a stable branch of finite-amplitude standing waves coexisting with the TW2 branch at $S = 3000$. This branch has been traced from $R = 3190$, a value subcritical to the Hopf bifurcation, to $R = 3220$. The SW is less vigorous than the TW, with the peaks of the oscillatory Nusselt numbers achieved being considerably smaller than the (steady) levels reached by the TW. One possible explanation for the coexistence of this SW branch and TW2 is that both subcritical branches have turning points which connect each unstable branch to stable ones. A bifurcation analysis, which has not yet been done, would help to clarify this point.

5. Constrained motion

We report results for constrained motion of two types, case $(A : L = 2)$ with boundary conditions (4) applied with $L = 2$, and case $(A : L = 1)$, being the same except $L = 1$. (Other examples with non-integer values of L not differing much from 2 and therefore close to the linearly most unstable oscillatory modes described in §2, have been calculated by Lele 1985, and yield qualitatively similar results.) Recall the 'wavenumber' parameter $q = 2/L$ that we have introduced. Application of constrained conditions (A) with sidewall boundaries separated by L permits the resolution of periodic motions with wavelength $2L$, or wavenumber $1/L$. Thus the subcase of $(A : L = 1)$ captures one cell (region of closed streamlines) of a periodic motion of wavenumber $q = 1$ at marginally supercritical conditions, while $(A : L = 2)$ can capture two counter-rotating cells of disturbances of wavenumber $q = 1$, but also one cell with wavenumber $q = 1/2$. When only one cell is included in the computational domain, the symmetries applied by K are realized, and the fixed

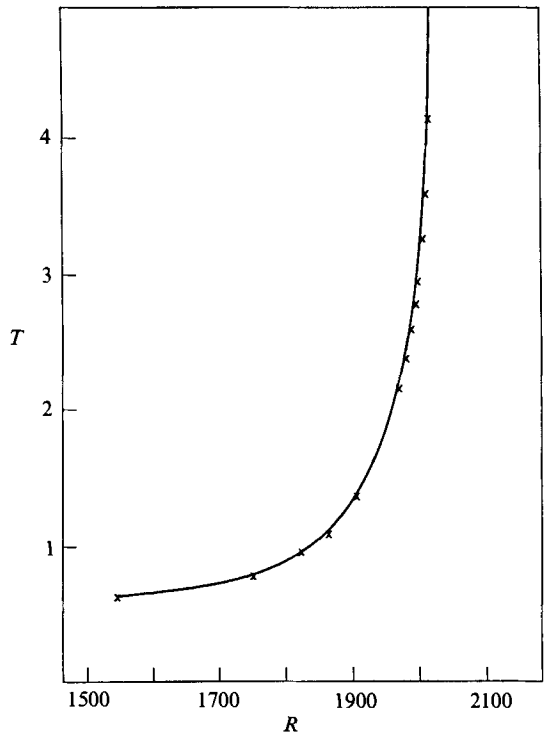

FIGURE 12. Variation of the (time) period, T, with R under constrained boundary conditions ($L = 1$) for $S = 1000$. Note the rapid increase of period, interpreted as an approach to a heteroclinic (infinite period) orbit.

sidewalls are boundaries of the cell. When two cells are included, there is an internal boundary dividing the two cells that is computed rather than being specified *a priori*, and this internal boundary need not be vertical or fixed in time, being movable by the existence of perturbations with $q = 1/2$: this case is therefore intermediate between the constrained and unconstrained conditions.

5.1. *Single mode motions*

The manner of disappearance of periodic motion suggests that we may be able to continue to realize oscillatory convection for $R \geqslant R^{\mathrm{HM}}$ at $S = 350$, provided the constraint of vertical stress-free boundaries is enforced. Computations with boundary conditions ($A : L = 1$) show this to be true. At $S = 350$, the period T of perturbations with fundamental wavenumber $q = 1$ increases as R increases, and $T \to \infty$ as $R \to R^{\mathrm{het}} \approx 1136$. Similar behaviour is found for $S = 500$ and $S = 1000$: figure 12 illustrates the latter case. Monotonic convection occurs for $R \geqslant R^{\mathrm{het}}$. The destruction of periodic motion in this way can be understood by reference to a local analysis of the five-mode system in the vicinity of the multiple bifurcation point $(S^{\mathrm{D}}, R^{\mathrm{D}})$. ML (in an analysis similar to that of Guckenheimer & Knobloch 1983) show that in the vicinity of this point, the five-mode system can be fully described by a subsystem with two-degrees of freedom. The periodic motion for each $R^{\mathrm{H}} < R < R^{\mathrm{het}}$ corresponds to a limit cycle contained within phase orbits connecting two saddle points (and thereby comprising a so-called heteroclinic orbit). The last possible periodic motion as R is increased is the heteroclinic orbit, which has infinite period.

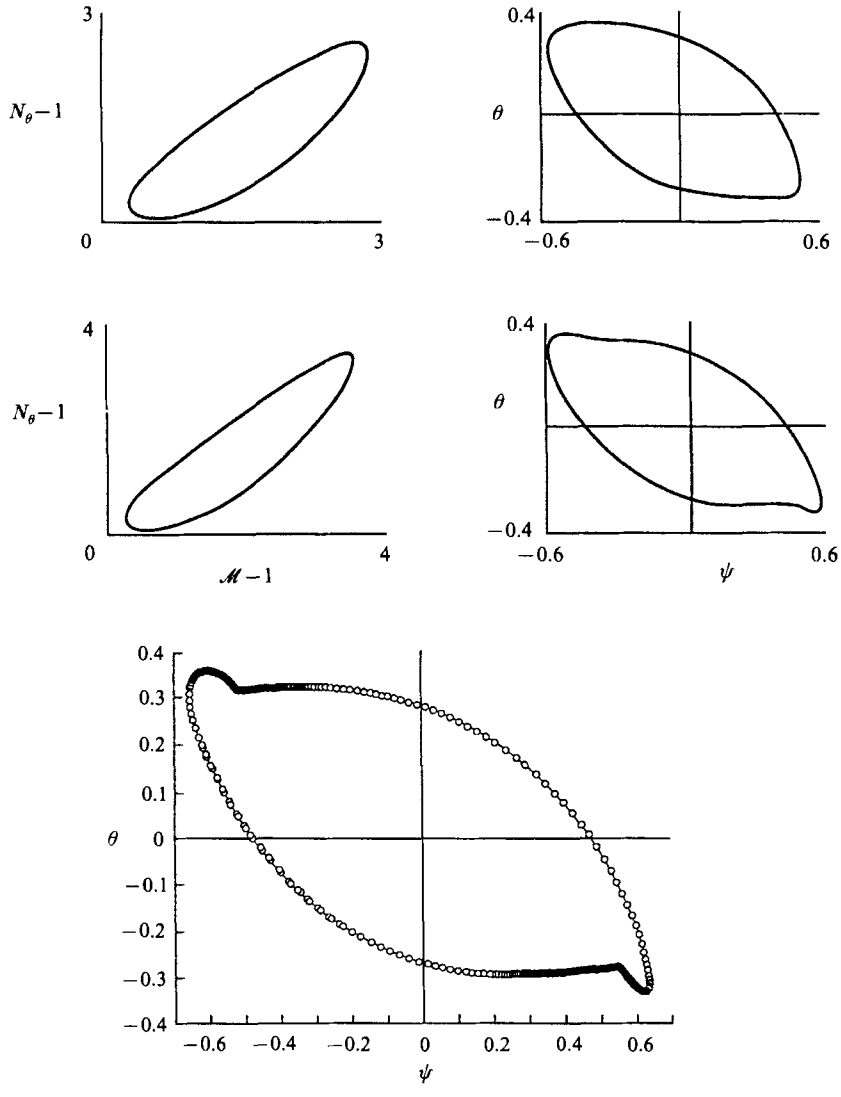

FIGURE 13. Orbits of limit cycles for $S = 350$, and constrained boundary conditions with $L = 1$. (*a*) Left and right panels are, respectively, projections onto the $(\mathscr{M}-1, N_\theta-1)$ (shifted) Nusselt-number plane and the (ψ, θ)-plane. Top pair is for $R = 1080$ and the bottom pair for $R = 1120$. (*b*) As in (*a*) for $R = 1134$, and showing the distribution of points visited during equal intervals of time.

For still larger values of R, the system is attracted to a fixed point, representing steady motion. This scenario is consistent with the behaviour we have described for the full partial differential equations. Further support for this explanation is to be had by examination of the projections of the phase portraits at $S = 350$ shown in figure 13. Two projections are shown, one is the locus of points traced out in time for the values of $\mathscr{M}-1$ and $N_\theta-1$, and the other is the locus of ψ and θ at a particular spatial point in our numerical grid. The grid used here is 16×16, and the point used for the projection (which we shall use again later) is the point $(3, 5)$. Figure 13(*a*) shows the development of the limit cycle for two values of R. Figure 13(*b*) shows a

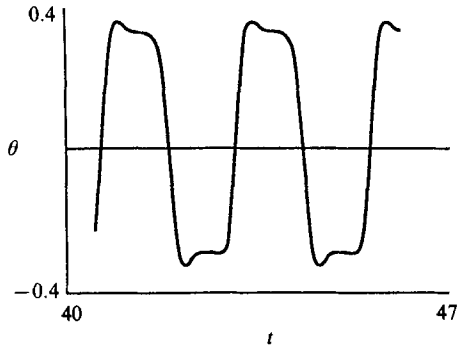

FIGURE 14. Time history of temperature perturbations for constrained ($L = 1$) conditions for $S = 350$, $R = 1130$.

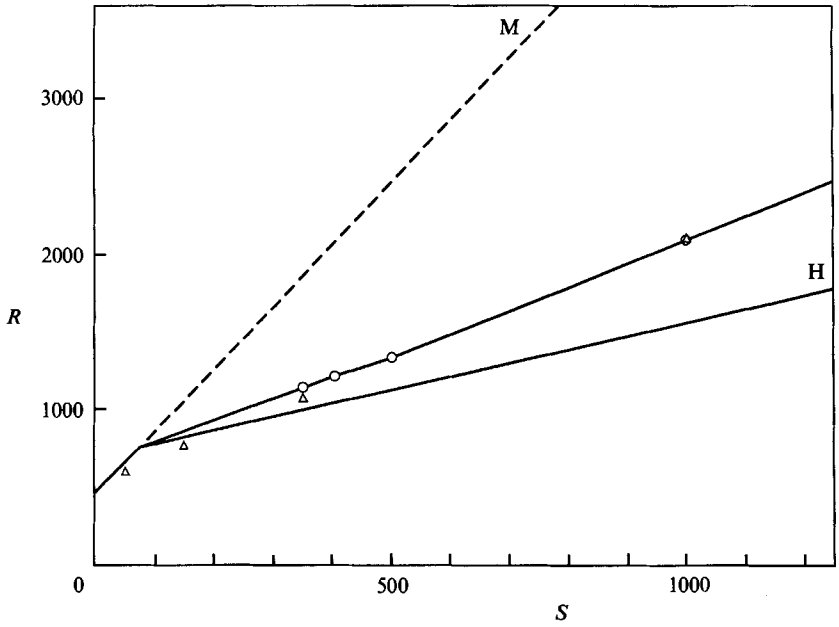

FIGURE 15. Regime diagram for $S \leqslant 1000$ under constrained boundary conditions ($L = 1$). Lines M and H mark onset of linear instability to monotonic and overstable convection. Triangles mark the locations of the computed turning points, $R_t(S)$, for steady convective states; the circles points, $R^{het}(S)$, where the period is estimated to reach infinity and a heteroclinic bifurcation is inferred. Steady convective states are subcritical relative to the onset of oscillatory convection for $S < 250$. For larger values of S, steady states are supercritical relative to the Hopf bifurcation, and may exist only for $R > R_t > R^H$. Note the apparent coalescence of $R^{het}(S)$ and $R_t(S)$ as S increases.

limit cycle at this value of S for a slightly larger R, but with dots placed at equal intervals of time. Portions of the curve with closely spaced dots are traversed slowly, as would occur in the vicinity of a saddle point, and the figure shows two intervals of densely packed dots. The time series for θ for $R = 1130$, in figure 14, shows the time behaviour associated with this flirtation with the saddle points.

The increase of period with increase of R, with singly periodic motion terminating at what appears to be a heteroclinic bifurcation succeeded by steady convection, continues as S increases. Figure 15 is a regime diagram summarizing our findings for

$S \leqslant 1000$ under conditions $(A:L=1)$. The straight lines marked M and H on this figure correspond to the onset of linear instability to monotonic and overstable convection, respectively, for wavenumber $q=1$ (corresponding, as above, to a pair of the cells computed under conditions $(A:L=1)$). The triangles mark the locations of the computed turning points, $R_t(S)$, on the branch of steady convective states; the circles mark the terminal points, $R^{het}(S)$, for oscillatory motion as estimated from numerical experiment. On the line drawn through this point, the period of oscillatory convection reaches infinity and a heteroclinic bifurcation is inferred. For $S < 250$ (approximately) steady convective states are subcritical relative to the onset of oscillatory convection. For larger values of S, steady states are supercritical relative to the Hopf bifurcation, and may exist only for $R > R_t > R^H$. Thus, for $S > 250$, there is a range of R for which only oscillatory motion can succeed the basic state.

Another feature of interest in figure 15 is the apparent coalescence of $R^{het}(S)$ and $R_t(S)$ as S increases. The degenerate situation arising from such a coalescence, if it indeed does occur, has not been observed before in studies of doubly diffusive systems. Preliminary analytical work which may provide some guidance as to possible behaviour in these circumstances has been done by Dangelmayr, Armbruster & Neveling (1985).

5.2. *Dynamics involving multiple spatial modes*

We now describe motions under $(A:L=2)$, and for S both smaller and larger than the intersection of the H1 and H2 Hopf boundaries. This choice of constrained conditions allows us to include spatial modes with both $q=1/2$ and $q=1$. Recall that, at the intersection point, the system has a double Hopf bifurcation. Disturbances with the fundamental wavenumber corresponding to L and those with its first harmonic are simultaneously unstable. In the vicinity of these double Hopf points, and perhaps even at points somewhat removed from them, dynamical behaviour deriving from interactions between the two modes may be expected. This has been explored, using boundary data $(A:L=2)$, by numerical traverses at $S=500$, 1000, 1200 and 3000. The H1, H2 intersection arises at $S \approx 1080$, so the linearly most unstable mode is the fundamental $q=1/2$ for $S=500$ and 1000, and the first harmonic $q=1$ for 1200 and 3000. We shall give results for the latter two cases only, and just summarize our findings for the first two cases.

Our numerical traverses were carried out as follows: for S fixed, the system was given a weak perturbation with equal amplitudes in wavenumbers $q=1/2$ and 1, with R set at a supercritical value leading to a limit cycle consistent with a Hopf bifurcation. This motion was then traced to successively higher values of R by incrementing R and using the solution last found as initial data. A grid spacing of 32×16 was used, and a time step of 0.001 was found adequate to describe transients: very long simulations, typically 200000 time steps, were required for a given point in parameter space.

At $S=1200$, our linear stability results determine the onset of the Hopf bifurcation corresponding to $q=1$ to be at $R=1710$ with angular frequency $\omega_1 = 67.67$, and that corresponding to $q=1/2$ to be at $R=1752$, with angular frequency $\omega_2 = 14.39$. For larger values of R, the frequencies associated with each of these modes will change, but we use the symbols ω_1 and ω_2 to designate frequencies that can be traced to the two Hopf onset frequencies; as these are quite different, no confusion in this interpretation is encountered. Time series and power spectra at $(S,R)=(1200,1740)$ show that the mode with the smaller frequency (i.e. ω_2,

associated with a perturbation having $q = 1/2$, which is linearly stable at this value of R) decays monotonically, and the system is attracted to a limit cycle with frequency ω_1. At $(S, R) = (1200, 1744)$, integration of the system to 100000 time steps again indicates attraction to the ω_1 limit cycle. A Poincaré section (ψ *vs.* θ taken at the section $N_\theta - 1 = 0.3$ – the figure is not displayed in this paper but may be found in Lele 1985) show a spiralling towards a fixed point on the Poincaré section, but with an interesting feature. The trajectory in this approach (for the time steps 80000–100000) appears to be locked onto 15 segments, so that 15 points are visited at each turn of the spiral. At the 100000th time step, when the calculation was terminated, the radius of the spiral is small. If the system is in fact attracted to a limit cycle, then each of the 15 sets of points will converge to the same fixed point. It appears likely that this will be the case. An alternative possibility is that each of the 15 sets approach distinct limit points, implying a frequency-locked periodic orbit on a 2-torus of small cross-section about the ω_1 limit cycle, and this cannot be ruled out without continuing the computation for significantly longer times.

Simulations at $(S, R) = (1200, 1748)$ were carried out to 140000 time steps, by which time the nature of the motion was clearly established to be a periodic, two-frequency locked state, involving elements of both ω_1 and ω_2. The projection of the state space trajectory onto the (ψ, θ)-plane (at the point (3, 5) in the grid) produced from the time interval between time steps 120000 and 140000 is shown in figure 16(*a*), and the Poincaré section (defined by the intersection, in either direction, of the section $N_\theta - 1 = 0.3$) for the same period is shown in figure 16(*b*). The asymptotic state is a limit cycle on a 2-torus. This limit cycle passes through the surface-of-section exactly 19 times in each direction, producing 19 points in the Poincaré section, after which time the process is repeated. Examination of the order in which these points are visited, the rotation number ρ, (see Iooss & Joseph 1980) was found to be 4/19, meaning that for 19 rotations about the larger dimension of the torus, the orbit passes around its smaller dimension exactly 4 times. The conclusions drawn from here were verified by examining other Poincaré sections, not shown. In addition, power spectra confirm this picture. For example, the power spectrum (see Lele 1985, where the spectrum is plotted against circular frequency $f = \omega/2\pi$) of ψ (at point (3, 5)) shows sharp peaks at $\omega_1 \approx 57.33 \pm 0.79$ and $\omega_2 \approx 11.78 \pm 0.79$ and additional peaks consistent with 4/19 frequency-locked periodic motion involving these two frequencies, the fundamental frequency of which is $\omega^* = \omega_1/19 = \omega_2/4$. The power spectrum of N_θ shows sharp peaks at $2\omega_1$ and $2\omega_2$ (Lele 1985); since N_θ is insensitive to the sense of the motion, this behaviour of the power spectrum also indicates motion with the frequencies ω_1 and ω_2, again confirming our conclusions.

Quasi-periodic two-frequency motion (that is, having two incommensurate frequencies) obtains at $(S, R) = (1200, 1750)$. Simulation at this point was carried out to 200000 time steps, which sufficed to conclude that the asymptotic state was indeed quasi-periodic. Figure 17(*a*) shows the state space trajectory in the (ψ, θ)-projection previously described, for the last 20000 time steps of the simulation, while figure 17(*b*) shows the Poincaré section, but now displaying points visited in the final 40000 time steps. The circles in figure 17(*b*) correspond to points crossing the surface-of-section during the final 20000 time steps, and the triangles mark crossings during the 20000 preceding time steps. Over most of the Poincaré section, the circles are phase shifted relative to the triangles, but both sets of points appear to fall on the same curve. If the simulation were to be continued, new points on the curve would be visited, eventually filling in a smooth, dense curve, indicative of a quasi-periodic orbit on the 2-torus. Power spectra again show two dominant frequencies and also

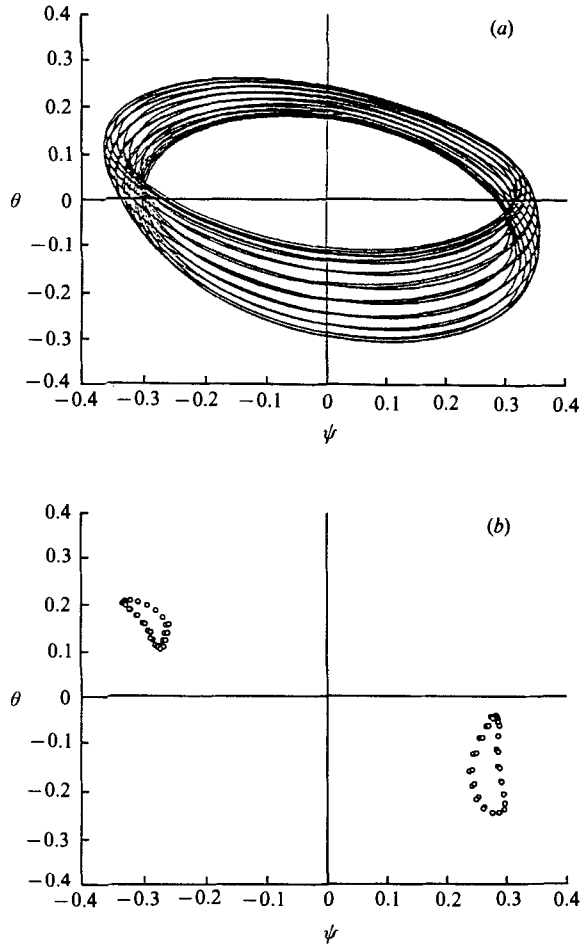

FIGURE 16. (*a*) Projection of the state space trajectory onto the (ψ, θ)-plane at point (3, 5) in the grid for $(S, R) = 1200, 1748)$. (*b*) Poincaré map at surface-of-section $N_0 - 1 = 0.3$ for the same period. The asymptotic state is a limit cycle on a 2-torus with rotation number $\rho = 4/19$.

peaks at sums and differences of the two principal frequencies (expressed as circular frequencies, these are $f_1 = 2.90 \pm 0.04$ and $f_2 = 0.60 \pm 0.04$) which are inferred to be incommensurate.

If R is increased to a value $(S, R) = (1200, 1754)$ just above the Hopf bifurcation point $(S, R) = (1200, 1752)$, quasi-periodic motion is lost, and the system is attracted to a single-period limit cycle. This is established by time-series and power spectra. In the simulations, the larger frequency (ω_1) signal decays monotonically, leaving only motion with frequency ω_2, corresponding to the nearby Hopf transition. We have looked at the spatial structure of the oscillatory motion remaining, and find only a single cell in our computational domain of $L = 2$, thus firmly connecting it with the $q = 1/2$ Hopf bifurcation. The loss of stability of the quasi-periodic state to a single-frequency limit cycle is consistent with the local unfoldings of Moroz & Leibovich (1987, generalizing, for the present problem, the analysis of five-mode system of §3 – and in particular ML – to the case of two spatial modes), and of Guckenheimer & Holmes (1983) and Moroz & Holmes (1985) for other finite-dimensional systems. In

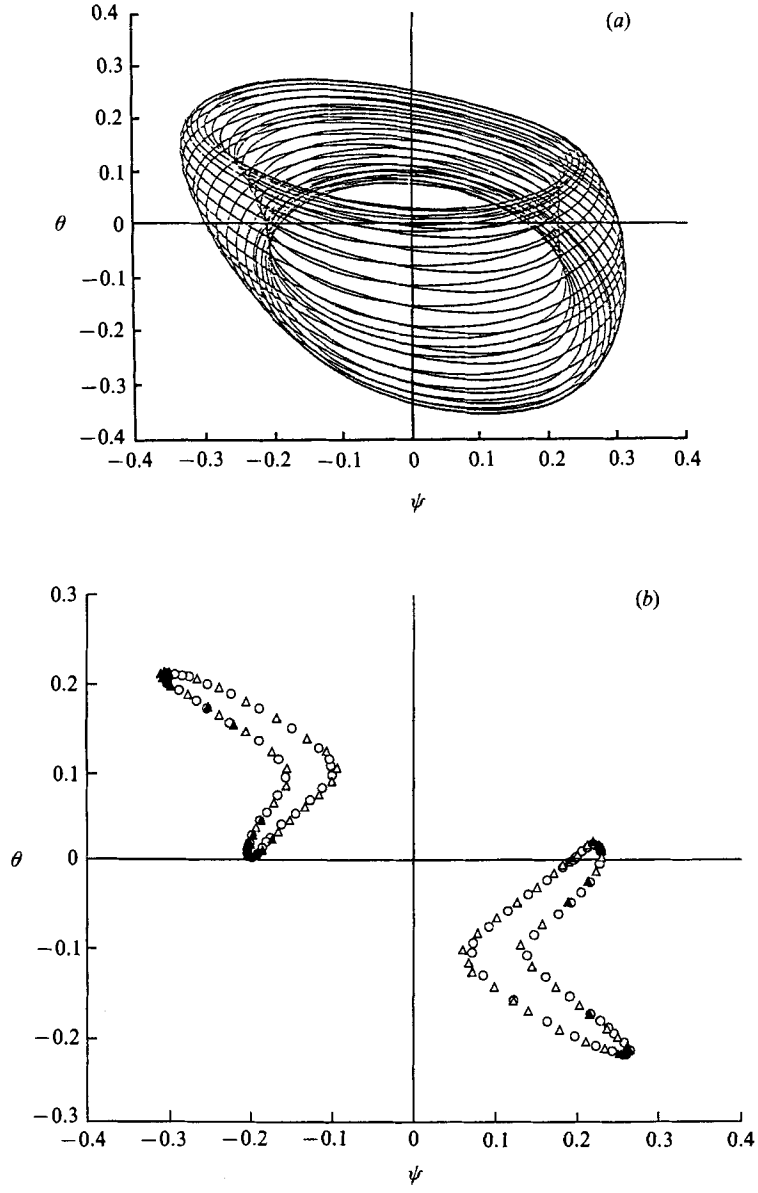

FIGURE 17. (*a*) State space trajectory in the (ψ, θ)-projection at $(S, R) = (1200, 1750)$ with quasi-periodic two-frequency motion. (*b*) Poincaré section: the circles correspond to points crossing the surface-of-section during the final 20000 time steps, and the triangles mark crossings during the 20000 preceding time steps, and are generally phase-shifted relative to the triangles, but fall on the same curve.

these analyses, the quasi-periodic state approaches the ω_2 limit cycle as a control parameter is increased, and merges with it at some critical value, beyond which only the ω_2 limit cycle is obtained. If R is increased sufficiently at $S = 1200$, all time dependence is lost, and the system evolves to steady convection.

We now turn to the traverse at $S = 3000$ under the constrained conditions $(A : L = 2)$. According to our linear stability calculations, the Hopf bifurcation point

R	Branch I description	Branch II description
3191	Hopf bifurcation, $T = 0.317$	Hopf bifurcation, $T = 0.317$
3540	SP, $T = 0.392$	—
3550	—	SP
3556	—	QP2T, not fully characterized
3560	—	P2T, $T^* = 46.4$
3580	—	P2T, $T^* = 15.19$, $\rho = 49/162$
3600	SP, $T = 0.409$	Not fully characterized, either QP2T or P2T with large fundamental period T^*
3610	SP, $T = 0.4055$	As at 3600
3612	—	P2T, $T^* = 14.67$, $\rho = 11/38$
3614	—	P2T, $T^* = 22.76$, $\rho = 50/77$
3615.4	—	P2T, $T^* = 2.70$, $\rho = 2/7$
3616	—	P2T, $T^* = 2.70$, $\rho = 2/7$
3620	QP2T, $\rho \approx 0.294$ (irrational)	P2T, $T^* = 2.71$, $\rho = 2/7$
3624	QP2T	P2T, $T^* = 2.72$, $\rho = 2/7$
3626	QP2T, $T_1 \approx 0.408$, $T_2 \approx 1.60$	—
3628	QP2T, $T_1 \approx 0.408$, $T_2 \approx 1.60$	P2T, $T^* = 2.72$, $\rho = 2/7$
3628.06	—	Intermittent chaos
3630	—	Intermittent chaos
3640	—	Intermittent chaos

TABLE 2. Types of motions computed under constrained conditions with $L = 2$

(H_2) at $S = 3000$ for disturbances with $q = 1$ occurs at $R = 3191$ with frequency $\omega_1 = 19.8$ (or period $T_1 = 2\pi/\omega_1 = 0.317$), and that for $q = 1/2$ (H_1) occurs at $R = 3827$ with frequency $\omega_2 = 4.9$ (or period $T_2 = 1.28$). Following the procedure already outlined for the traverse at $S = 1200$, we explored the dynamical behaviour as R is increased from R^H. Briefly, we find the single-period (SP) motion branching at the Hopf bifurcation point of $R = 3191$ to persist to $R = 3610$ on what we designate as branch I. Somewhere between this value and 3620 on branch I, the limit cycle loses stability to a quasi-periodic 2-torus (abbreviated subsequently as QP2T) wrapped around the limit cycle. Motion on this QP2T has been traced up to $R = 3628$, but it coexists with other attractors to be described. We have not attempted to track the QP2T on branch I to values of R larger than 3628. The limit cycle branching at the Hopf bifurcation point can also lose stability, at $R = 3550$, to other perturbations. We call this branch II. The states arising include a QP2T distinct from that on branch I, followed, as R is increased, by a sequence of states attracted to periodic motion on a 2-torus (P2T) with different (rational) frequency-locking ratios: subsequent bifurcations of this branch lead to chaotic states. The system behaviours we have found are listed in table 2 according to the branch from which they stem. Bifurcations along each of these two main branches are inferred at points separating intervals of R with qualitatively distinct features. In some cases, we indicate the period: if the attractor is a frequency-locked state, the period given is T^*, the fundamental period, and, where given, ρ is the rotation number (the ratio of the two locked frequencies), which was determined from the order that points are laid down on the Poincaré section as previously described.

Clearly, the sequence of events on branch II is more complex than on branch I, as the latter seems to have only singly periodic and two-frequency quasi-periodic states. Consequently, we shall illustrate only the characteristics of solutions found on branch II.

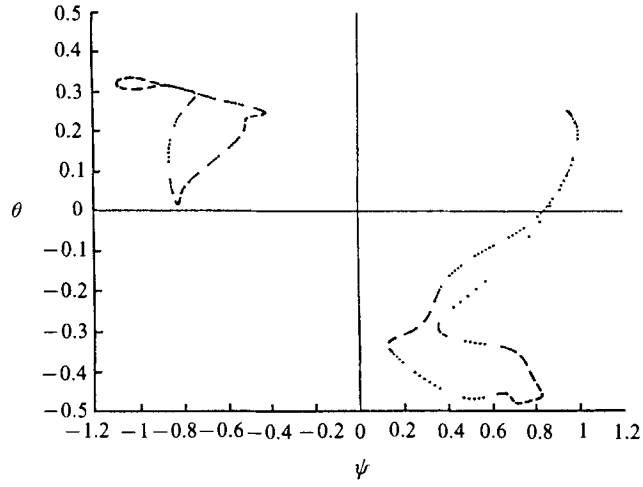

FIGURE 18. Poincaré surface-of-section at $N_\theta - 1 = 1$ with $S = 3000$, $R = 3556$. Plot is projection on the (ψ, θ)-plane. The continuous segments in the figure indicate a 2-period quasi-periodic solution.

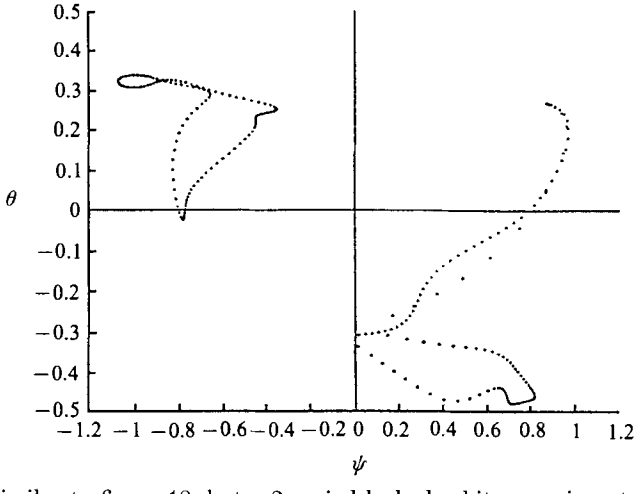

FIGURE 19. Similar to figure 18, but a 2-period locked orbit occurring at $S = 3000$, $R = 3560$: each point in the Poincaré plot has been visited twice.

Figure 18 is a Poincaré surface of section (taken at $N_\theta - 1 = 1$) at $R = 3556$. From the seemingly continuous segments in the figure, we believe it to be a 2-period quasi-periodic solution. Figure 19 shows the corresponding picture for the 2-period locked orbit occurring at $R = 3560$: each point in the Poincaré plot has been visited twice. Figure 20(*a*) at $R = 3580$ is similar, and shows a 2-period locked motion, with $T_1/T_2 = 49/162$. The fundamental period T^* was determined precisely by following the system through four repetitions of the Poincaré plot. The Fourier transform of the time series of ψ in figure 20(*b*), taken over four periods of the fundamental, shows the constituent (circular) frequencies $f_1 = 1/T_1$ and $f_2 = 1/T_3$, as well as the fundamental $f^* = 1/T^*$. These pictures are very similar at $R = 3612$ (which we do not show), but the locking ratio there is 11/38.

What we identify as intermittently chaotic states arise from a frequency-locked

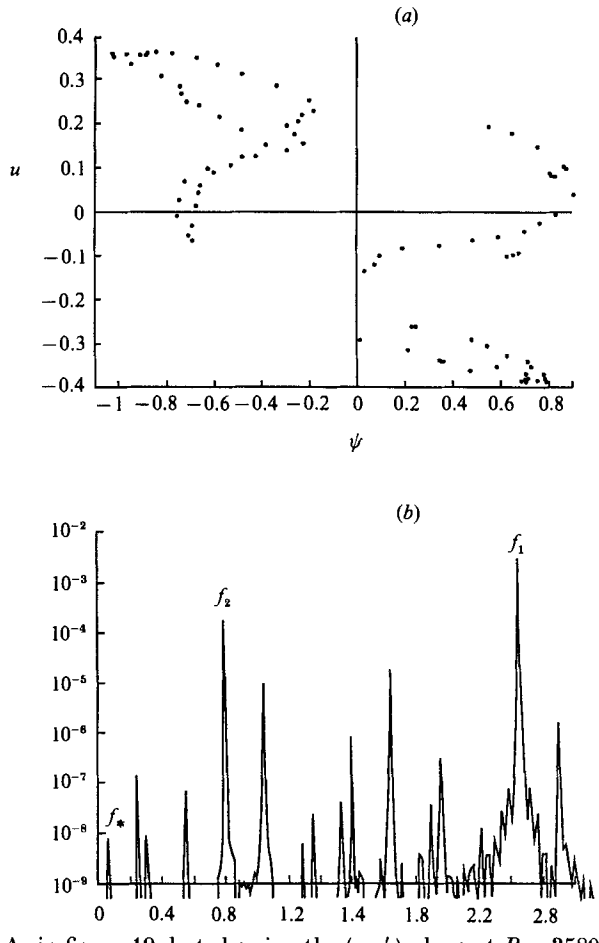

FIGURE 20. (*a*) As in figure 19, but showing the (u, ψ)-plane at $R = 3580$. This is a 2-period locked motion, with rotation number = 49/162. (*b*) Fourier transform of ψ. The constituent frequencies $f_1 = 1/T_1, f_2 = 1/T_2$, and fundamental $f^* = 1/T^*$ are marked.

state with locking ratio 2/7. This ratio is maintained for an interval of R that seems to extend from about 3615 to 3628. The ψ–u and $N_\theta - 1$ *vs.* $\mathscr{M} - 1$ projections of the 2/7 orbit at $R = 3624$ are shown in figure 21: the tracing and retracing of the seven big loops in the θ–u projection can easily be followed. Time traces for $N_\theta - 1$ and for ψ are shown in figure 22.

The 2/7 locked periodic state that persists to $R = 3628$ is succeeded at $R = 3628.06$ by an apparently intermittently chaotic state. Figure 23 shows the time series of ψ at this transition to chaos (the time series is compressed by displaying only those values of ψ at crossings of the Poincaré section $N_\theta - 1 = 1$) as well as at $R = 3628.2$ and 3628.4. Here the characteristics of the 2/7 locked periodic state remain evident, but the trace is interrupted at irregular times and for irregular durations by non-periodic 'bursts'. The windows marked A have the features of a 2/7 periodic orbit. Windows marked B correspond to bursts, excursions of the system to other regions of phase space before returning to the weakly unstable states associated with the 2/7 orbit. As R is increased, the fraction of time spent in the ordered state decreases. Windows marked C also appear to be explicable as significant time spent by the

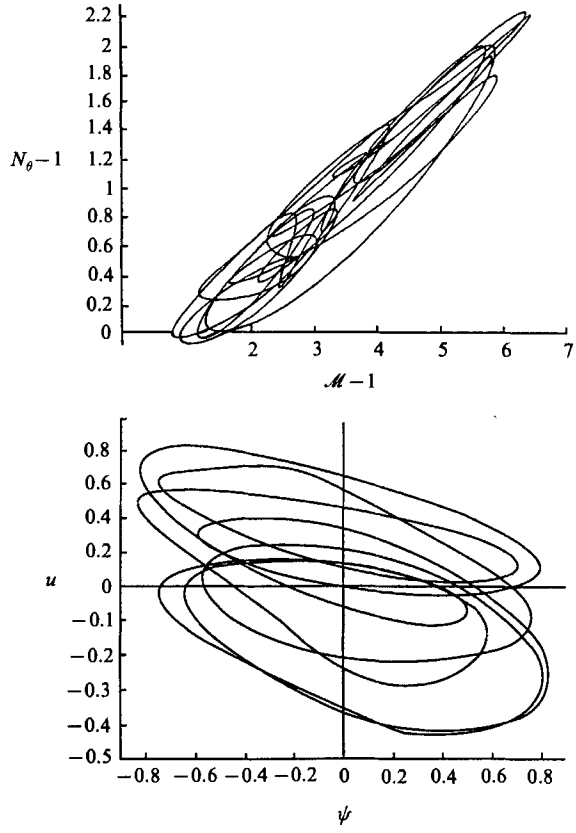

FIGURE 21. ψ *vs.* u and $N_\theta - 1$ *vs.* $\mathcal{M} - 1$ projections of the frequency-locked state at $R = 3624$. The orbit has rotation number $\rho = 2/7$.

system close to a periodic or quasi-periodic orbit, but one different in character from the underlying 2/7 orbit. Recalling the coexisting quasi-periodic orbit available, branch I, at these value of R leads to one possibility, but we have no evidence to support this suggestion.

The Poincaré plot (of θ *vs.* ψ, for 120 time units or 120000 time steps) in figure 24 shows the chaotic state at $R = 3630$. The corresponding ψ spectrum in figure 25 shows strong peaks at the frequencies of the 2/7 locked state, but a comparison with spectra computed for the demonstrably 2/7 locked states shows an increase in *broadband* background levels by two orders of magnitude.

The transition to chaos shown here appears consistent with the Pomeau–Manneville (1980) type-I intermittent transition. The characteristics of this kind of transition are as follows: an ordered (periodic) motion loses stability at a parameter value R_c to a state in which bursts interrupt the ordered motion. Near the bifurcation point, the mean interval between bursts is predicted to vary in proportion to $(R - R_c)^{-\frac{1}{2}}$, but the burst amplitude does not change appreciably. Aside from the qualitative similarity in the present system behaviour and this scenario, the only corroboration of our impressions immediately available to us is the variation of mean interval between bursts with R, and even here there is both a subjective element (in the decision on the time of onset of bursting and the time of return to order) and too small a sample of data points to lead to a convincing determination. Nevertheless,

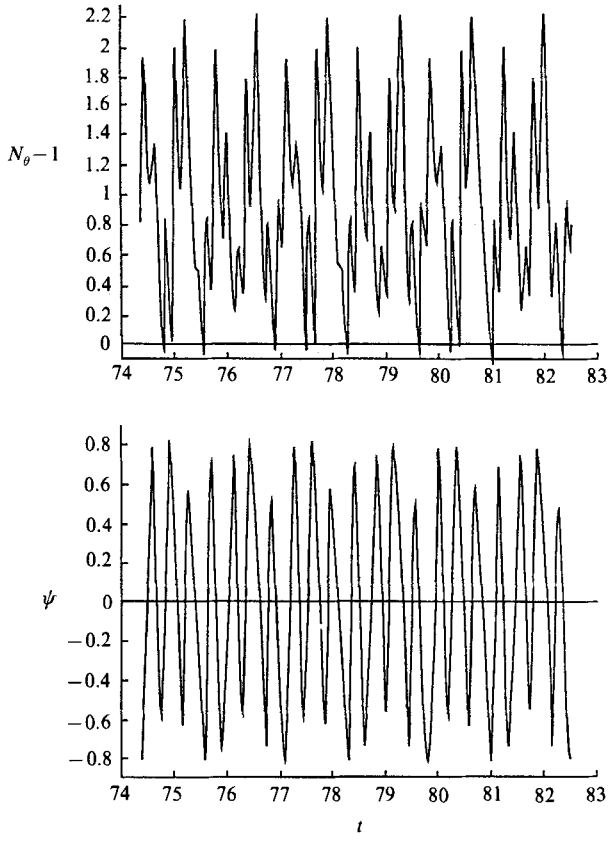

FIGURE 22. Time traces of $N_\theta - 1$ and of ψ for motion shown in figure 21.

if we use the three records shown in figure 23 to estimate the time spent in state A, controlled by the underlying 2/7 attractor, we find it consistent with the square-root behaviour, the time being approximately given by $11.2(R-R_c)^{-\frac{1}{2}}$, with $R_c \approx 3627.91$.

Before leaving this subsection, it is important to again emphasize that the complex motions reported here and summarized in table 2 exist only when the symmetries associated with the constrained boundary conditions (here with $L = 2$, permitting two spatial harmonics to interact) are enforced. When these are relaxed to require only spatial periodicity, the temporally complex states are expected to be unstable and therefore unrealizable. This expectation was directly verified in one case. Beginning with the 2/7 locked orbit as initial data, the computations were continued with spatially periodic boundary conditions, and the system evolved to a steady state.

6. Concluding remarks

Previous computations of thermal convection by Curry *et al.* (1984) have shown that the relaxation of lateral symmetry conditions leads to a significant reduction of the Rayleigh number for transition to periodic convection in two dimensions, but they did not uncover qualitatively different dynamical behaviour resulting from a change of lateral boundary conditions. (More significant qualitative changes were

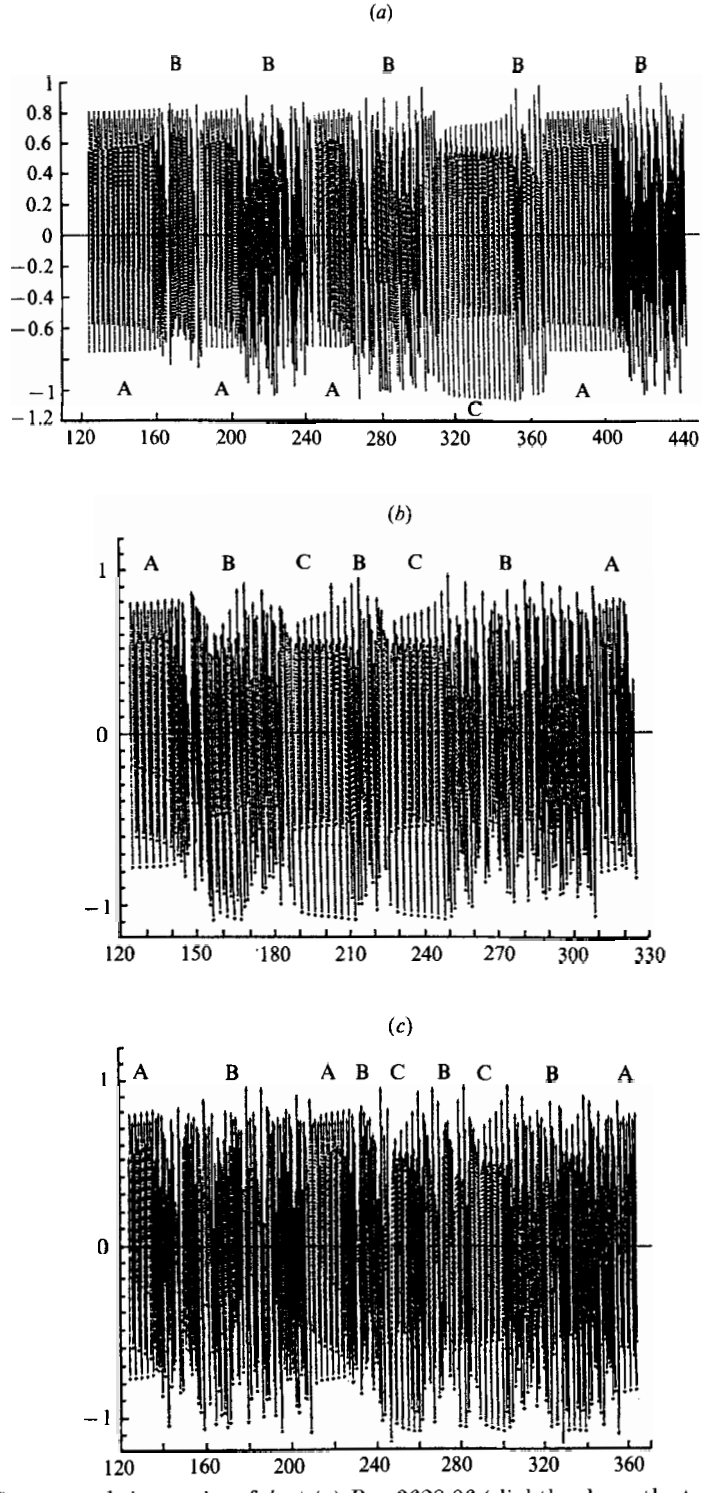

FIGURE 23. Compressed time series of ψ at (*a*) $R = 3628.06$ (slightly above the transition to chaos). (*b*) $R = 3628.2$, (*c*) $R = 3628.4$. Characteristics of the 2/7 locked periodic state remain evident, in windows marked A. Windows marked B correspond to disordered bursts. Those marked C also appear ordered, but different from A.

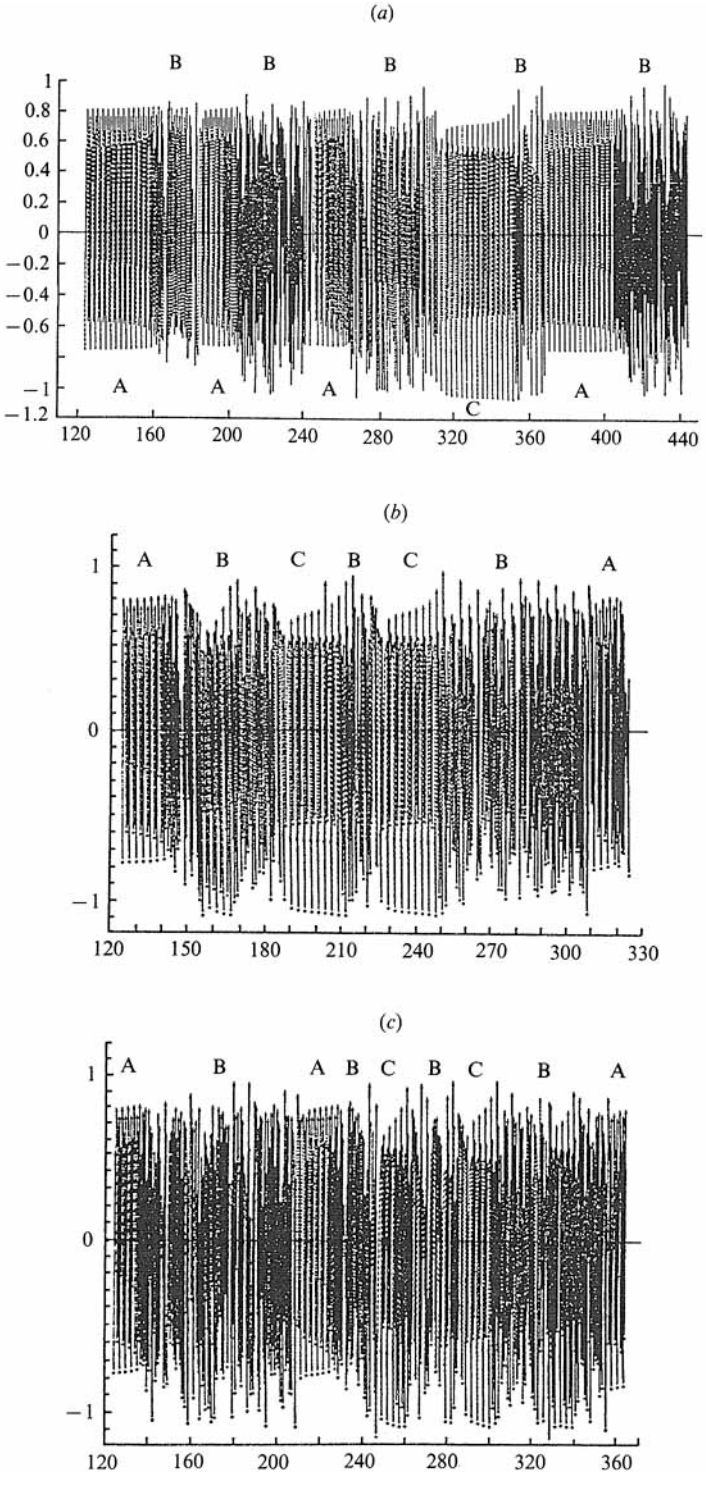

FIGURE 23. Compressed time series of ψ at (*a*) $R = 3628.06$ (slightly above the transition to chaos). (*b*) $R = 3628.2$, (*c*) $R = 3628.4$. Characteristics of the 2/7 locked periodic state remain evident, in windows marked A. Windows marked B correspond to disordered bursts. Those marked C also appear ordered, but different from A.

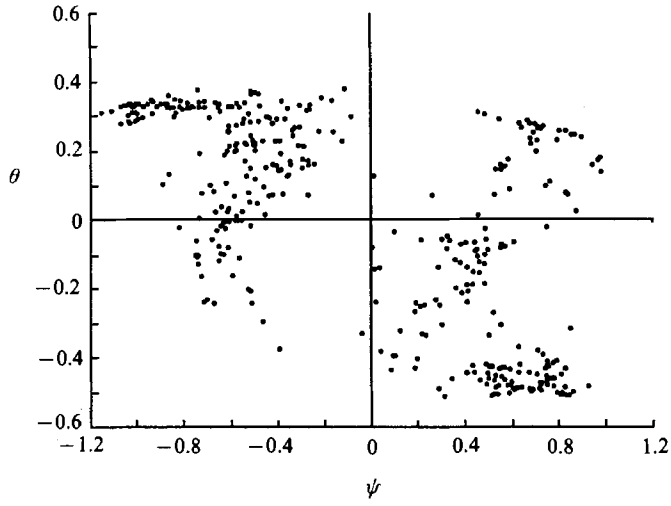

FIGURE 24. Poincaré plot in (ψ, θ)-projection, chaotic state at $R = 3630$.

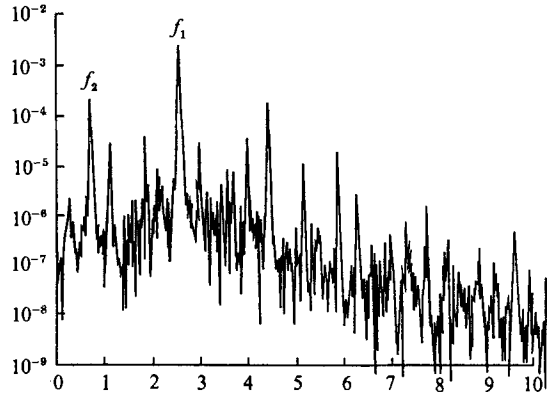

FIGURE 25. ψ-spectrum for case shown in figure 24. Note strong peaks at the frequencies of the 2/7 locked state, but also the development of broadband noise.

found in going from two to three dimensions, the important effect of this change being the major point of their paper.)

An important general lesson learnt from the present study is that innocent alterations of lateral boundary conditions and symmetry conditions in the horizontal, as well as conditions on the top and bottom planes, can lead to qualitatively different behaviour at least in problems of doubly diffusive type. Most are aware of the significance of the choice of conditions at the top and bottom of the fluid layer, but this is often not true of lateral conditions. The imposition of symmetry conditions is a tempting and commonly adopted way of stretching computational resources at no apparent additional cost: it therefore is important to appreciate that the solutions so obtained will not be realizable in many problems of interest. In particular, whenever any existing lateral constraints are separated by distances large compared with the layer depth – as would generally be the case with Langmuir circulations as well as many thermosolutal problems – the symmetry conditions or constrained lateral boundary conditions are physically unrealistic, and periodic conditions

should be used instead. We therefore regard the solutions found under constrained (no-flux) lateral boundary conditions to be physically unrealizable for Langmuir circulations, except possibly in unusual circumstances.

The replacement of the isothermal boundary condition of the 'ideal double-diffusion' (IDD) problem by constant heat flux at the top and bottom planes results in lower critical Rayleigh numbers for destabilization of the rest state. In the sense that this replacement imposes less severe constraints on the system, this effect is not unexpected. When periodic lateral boundary conditions are imposed in the present problem, however, there are added dynamical possibilities. In the overstable regime, the most complex time dependence to emerge, in both the ideal double-diffusion problem and the present one, is a limit cycle. On the other hand, this may exist in two stable forms, both a standing wave and a travelling wave, or alternatively, stable travelling waves may coexist with stable steady states. Initial conditions will determine which of the coexisting stable states will be realized. These possibilities do not arise in the IDD problem. When constrained, no-flux, lateral boundary conditions are imposed, more complex dynamics are possible in both problems, but the resulting time-dependent motions are qualitatively different. Period doubling occurs in IDD but not in the constant-heat-flux or Langmuir circulation case, which instead yields either two-frequency locked, or two-frequency quasi-periodic, or intermittently chaotic motion.

In all cases, if the destabilizing Rayleigh number R is increased sufficiently (the precise value increasing with the stabilizing Rayleigh number S), steady convection is expected to result. Physically, this just implies that as the convection and resulting overturning of isotherms in the LC case (or stabilizing solute contours in the double-diffusion case) increases, the restoring buoyancy force due to the stabilizing agent is reduced, in effect reducing S in the bulk of the fluid to values too low to admit oscillatory convection. The steady convection that results is subcritical (with respect to monotonic convection) and is more deeply subcritical when periodic boundary conditions are imposed than it is when constrained boundary conditions are imposed.

In the two-dimensional Langmuir circulation case, time-dependent convection is possible only in a modest range of supercritical Rayleigh numbers. This suggests why the visible surface windrows that serve as the hallmark for Langmuir circulations are so prominent and prevalent. The organization of surface tracers into windrows is favoured by steady convective motions, and may be impossible, or at least weak and erratic, under conditions of oscillatory convection. Oceanic conditions are likely to be supercritical but unlikely to fall in the fairly small window that permits oscillatory convection. Thus, steady convection is the expected form of Langmuir circulations, at least in two-dimensions and subject to the other idealizations made in posing our theoretical model.

The possibility of travelling waves, which according to the results here should propagate rather slowly, leads to one possible explanation for observations of Langmuir circulation windrows that drift sideways to the wind. The present results suggest that this mode of drift will be possible only under conditions which are not highly supercritical and for which density stratification exists and survives the mixing accomplished by the Langmuir circulations.

We are greatly indebted to Nigel Weiss, who found an important misinterpretation in an earlier draft of our paper. This work was supported by the Physical Oceanography Program of the National Science Foundation under Grant

OCE8310624, and by the US Office of Naval Research under contract SRO IV. Additional support was provided by the US Army Research Office through the Mathematical Sciences Institute of Cornell University, and by a NATO Collaborative Grant to S. Leibovich and I. M. Moroz. Computing facilities were provided by the National Science Foundation through the Cornell National Supercomputer Facility, as well as the IMAP facility provided by IBM to Cornell University's Sibley School of Mechanical and Aerospace Engineering.

Appendix

We outline the salient features of our numerical procedures. More detail can be found in Lele (1985).

The governing equations (2) are first slightly recast before introducing the finite-difference approximations used to solve them. Anticipating that the numerical problem will be posed on a computational domain of width L in the y-direction, and that periodic solutions in y with wavelength L will be of particular interest, the following decompositions are introduced:

$$u(y,z,t) = \langle u\rangle(z,t) + u'(y,z,t), \quad \theta(y,z,t) = \langle\theta\rangle(z,t) + \theta'(y,z,t),$$

where

$$\int_0^L u'(y,z,t)\,\mathrm{d}y = \int_0^L \theta'(y,z,t)\,\mathrm{d}y = 0,$$

identifies $\langle u\rangle(z,t)$ and $\langle\theta\rangle(z,t)$ to be the cross-stream averages of u and θ, respectively, while $u'(y,z,t)$ and $\theta'(y,z,t)$ represent fluctuations about these average values. It should be recalled that u and θ represent perturbation fields to the nonconvective equilibrium state.

The equations governing the mean and fluctuating fields may be obtained from (2) by first taking their y-averages and subtracting the averaged from the original equations. Boundary conditions requiring periodicity over L are used to simplify the results. The resulting set of equations is discretized over a staggered, uniform grid. Different terms in the equations are discretized differently; all approximations, however, are second-order accurate. In constructing our approximation schemes we have followed the work of Orszag (1971), Williams (1969) and Piacsek & Toomre (1980).

The Jacobian $\mathrm{J}(\psi,\zeta)$ is discretized using the quadratic conserving scheme developed by Arakawa (1966), which has the advantage of exactly conserving the finite-difference analogues of vorticity, mean-square vorticity (enstrophy), and kinetic energy of motion in the (y,z)-plane. The Jacobians $\mathrm{J}(\psi,u')$ and $\mathrm{J}(\psi,\theta')$ are discretized using the scheme developed by Lilly (1965), which provides exact conservation of the finite-difference analogues of x-momentum, heat, mean-square temperature fluctuation, and kinetic energy associated with the x-velocity component u' on the staggered grid. All diffusion terms are approximated using standard central differences.

A two-step time advancement is used that provides formal second-order-accurate ($O(\Delta t)^2$) results. To avoid the time-step restriction on the stability associated to an explicit treatment of the diffusion terms, a time-splitting method (see Roache 1976, or the appendices of Orszag & Patera 1983, for details) is adopted. Briefly, the field is advanced in two steps, with diffusive terms accounted for in one step and non-diffusive terms in the other. This procedure introduces additional truncation errors. As argued by Orszag & Patera (1983), if each of the steps individually has a formal

accuracy of $O(\Delta t)^2$, then the overall error in the advance is $O(\Delta t)^{\frac{3}{2}}$. Orszag and his co-workers reduce this error by using a local Richardson extrapolation with every time step. We instead use a simple averaging scheme to reduce the error. The field is advanced by accounting first for the diffusive terms only, then for the non-diffusive terms only, and then the process is repeated in the opposite order. After these two separate time advances have been executed, the results are averaged, and our experience indicates that the time-splitting errors are significantly reduced. The partial advances accounting for non-diffusive terms are carried out by a standard Adams–Bashforth scheme, while the advances of diffusive terms is done by an efficient Alternating Direction Implicit (ADI) method (see Roache 1976). Details of the implementation are described in Lele (1985) (note two lines are inadvertently omitted from his figure A.4, which summarizes this part of the algorithm).

The Poisson equation relating the stream function to the vorticity field is solved by using the direct Poisson solver developed at NCAR by Swartztrauber & Sweet (1975), which provides the stream-function field to machine accuracy.

Our computer code was validated by solving a set of test problems which permit exact solutions, as well as known non-trivial fluid mechanical problems. The test problems include simple problems of diffusion, advection by a known velocity field, Rayleigh–Taylor instability (of a statically unstable density field) in various inviscid/viscous and non-diffusive/diffusive configurations, linear and nonlinear Bénard convection with simple boundary conditions, and double-diffusive convection with simple boundary conditions. The accuracy and convergence performance of the code were considered acceptable; details may be found in Lele (1985).

REFERENCES

Arakawa, A. 1966 Computational design for long-term numerical integration of the equations of motion: two-dimensional incompressible flow. Part. 1. *J. Comput. Phys.* **1**, 119–143.

Baines, P. G. & Gill, A. E. 1969 On thermohaline convection with linear gradients. *J. Fluid Mech.* **37**, 289–306.

Craik, A. D. D. 1977 The generation of Langmuir circulations by an instability mechanism. *J. Fluid Mech.* **81**, 209–223.

Craik, A. D. D. 1982 The drift velocity of water waves. *J. Fluid Mech.* **116**, 187–205.

Craik, A. D. D. & Leibovich, S. 1976 A rational model for Langmuir circulations. *J. Fluid Mech.* **73**, 401–426.

Curry, J. H., Herring, J. R., Loncaric, J. & Orszag, S. A. 1984 Order and disorder in two- and three-dimensional Bénard convection. *J. Fluid Mech.* **147**, 1–38.

da Costa, L. N., Knobloch, E. & Weiss, N. O. 1983 Oscillations in double-diffusive convection. *J. Fluid Mech.* **109**, 25–43.

Dangelmayr, G., Armbruster, D. & Neveling, M. 1985 A codimension three bifurcation for the laser with saturable absorber. *Z. Phys.* B **59**, 365–370.

Glendinning, P. & Sparrow, C. 1984 Local and global behaviour near homoclinic orbits. *J. Statist. Phys.* **35**, 645–696.

Golubitsky, M. & Stewart, I. N. 1985 Hopf bifurcation in the presence of symmetry. *Arch. Rat. Mech. Anal.* **87**, 107–165.

Guckenheimer, J. & Holmes, P. J. 1983 *Nonlinear Oscillations, Dynamical Systems, and Bifurcations of Vector Fields*. Springer.

Guckenheimer, J. & Knobloch, E. 1983 Nonlinear convection in a rotating layer: Amplitude expansions and centre manifolds. *Geophys. Astrophys. Fluid Dyn.* **23**, 247–272.

Huppert, H. E. & Moore, D. R. 1976 Nonlinear double-diffusive convection. *J. Fluid Mech.* **78**, 821–852.

Iooss, G. & Joseph, D. D. 1980 *Elementary Stability and Bifurcation Theory*. Springer.

KNOBLOCH, E. 1986 On the degenerate Hopf bifurcation with circular symmetry. In *Multiparameter Bifurcation Theory* (ed. M. Golubitsky & J. Guckenheimer). Contemporary Mathematics, vol. 56, pp. 193–201. American Mathematical Society.

KNOBLOCH, E., DEANE, A. E., TOOMRE, J. & MOORE, D. R. 1986*a* Doubly diffusive waves. In *Multiparameter Bifurcation Theory* (ed. M. Golubitsky & J. Guckenheimer). Contemporary Mathematics, vol. 56, pp. 203–216. American Mathematical Society.

KNOBLOCH, E., MOORE, D. R., TOOMRE, J. & WEISS, N. O. 1986*b* Transitions to chaos in two-dimensional double-diffusive convection. *J. Fluid Mech.* **166**, 409–448.

LAMB, H. 1932 *Hydrodynamics*, 6th edn, p. 372. Dover.

LANGMUIR I. 1938 Surface motion of water induced by wind. *Science* **87**, 119–123.

LEIBOVICH, S. 1977*a* Convective instability of a stably stratified water in the ocean. *J. Fluid Mech.* **82**, 561–585.

LEIBOVICH, S. 1977*b* On the evolution of the system of wind drift currents and Langmuir circulations in the ocean. Part 1. Theory and averaged current. *J. Fluid Mech.* **79**, 715–743.

LEIBOVICH, S. 1983 The form and dynamics of Langmuir circulations. *Ann. Rev. Fluid Mech.* **15**, 391–427.

LEIBOVICH, S. 1985 Dynamics of Langmuir circulations in a stratified ocean. In *The Ocean Surface* (ed. Y. Toba & H. Mitsuyasu), pp. 457–464. Reidel.

LELE, S. K. 1985 Some problems in hydrodynamic stability arising in geophysical fluid dynamics. Ph.D. dissertation, Cornell University.

LILLY, D. K. 1965 On the computational stability of numerical solutions of time-dependent non-linear geophysical fluid dynamics problems. *Mon. Weather Rev.* **93**, 11–26.

MARCUS, P. S. 1981 Effects of truncation in modal representations of thermal convection. *J. Fluid Mech.* **103**, 241–255.

MEYER, G. E. 1969 A field study of Langmuir circulations. In *Proc. 12th Conf. Great Lakes Res. Intl Assoc. Great Lakes Res.*, pp. 652–663.

MOORE, D. R., TOOMRE, J., KNOBLOCH, E. & WEISS, N. O. 1983 Period doubling and chaos in partial differential equations for thermosolutal convection. *Nature* **303**, 663–667.

MOROZ, I. M. 1985 Heteroclinic orbits in a model for Langmuir circulations. *Phys. Lett.* **110A**, 109–112.

MOROZ, I. M. 1986 Codimension-three bifurcations arising in Langmuir circulations. In *Multiparameter Bifurcation Theory* (ed. M. Golubitsky & J. Guckenheimer). Contemporary Mathematics, vol. 56, pp. 223–235. American Mathematical Society.

MOROZ, I. M. & HOLMES, P. J. 1985 Double Hopf bifurcation and quasi-periodic flow in a model for baroclinic instability. *J. Atmos. Sci.* **41**, 3147–3159.

MOROZ, I. M. & LEIBOVICH, S. 1985 Competing instabilities in a nonlinear model for Langmuir circulations. *Phys. Fluids* **28**, 2050–2061.

MOROZ, I. M. & LEIBOVICH, S. 1987 Codimension-two Hopf bifurcations in a model for Langmuir circulations. *Proc. Intl Conf. Fluid Mech.*, pp. 157–162. Peking University Press.

NIELD, D. A. 1967 The thermohaline Rayleigh–Jeffreys problem. *J. Fluid Mech.* **29**, 545–558.

ORSZAG, S. A. 1971 Numerical simulation of incompressible flows within simple boundaries: accuracy. *J. Fluid Mech.* **49**, 75–112.

ORSZAG, S. A. & PATERA, A. 1983 Secondary instability of wall bounded shear flows. *J. Fluid Mech.* **128**, 347–385.

PIASCEK, S. A. & TOOMRE, J. 1980 Nonlinear evolution and structure of salt fingers. In *Marine Turbulence* (ed. J. Nihoul), pp. 193–219. Elsevier.

POMEAU, Y. & MANNEVILLE, P. 1980 Intermittent transition to turbulence in dissipative dynamical systems. *Commun. Math. Phys.* 74, 189–197.

ROACHE, P. J. 1976 *Computational Fluid Dynamics*, 2nd edn. Hermosa.

SCHECTER, S. 1976 Bifurcations with symmetry. In *The Hopf Bifurcation and its Applications* (ed. J. Marsden & M. McCracken), pp. 224–249. Springer.

STERN, M. E. 1960 The 'salt fountain' and thermohaline convection. *Tellus* **12**, 172–175.

SWARTZTRAUBER, P. & SWEET, R. 1975 Efficient Fortran subprograms for the solution of elliptic partial differential equations. *NCAR Tech. Note* IA-109, Nat. Center for Atmos. Res., Boulder.

THORPE, S. A. 1985 Small-scale processes in the upper ocean boundary layer. *Nature* **318**, 512–522.

THORPE, S. A. & HALL, A. J. 1982 Observations of the thermal structure of Langmuir circulations. *J. Fluid Mech.* **114**, 237–250.

THORPE, S. A. & HALL, A. J. 1983 The characteristics of breaking waves, bubble clouds, and near-surface currents observed using side-scan sonar. *Continental Shelf Res.* **1**, 353–384.

VAN STRAATEN, L. M. J. U. 1950 Periodic patterns of rippled and smooth areas on water surfaces, induced by wind action. *Koninklijke Nederlandse Akademie der Wetenschappen* B**53**, 1217–1227.

VERONIS, G. 1965 On finite amplitude instability in thermohaline convection. *J. Mar. Res.* **23**, 1–17.

WILLIAMS, G. P. 1969 Numerical integration of the three-dimensional Navier–Stokes equations for incompressible flow. *J. Fluid Mech.* **37**, 727–750.

WELLER, R. A., DERAN, J. P., MARRA, J., PRICE, J. F., FRANCIS, E. A. & BOARDMAN, D. C. 1985 Three-dimensional flow in the upper ocean. *Science* **227**, 1552–1556.

WELLER, R. A. & PRICE, J. F. 1988 Langmuir circulation within the oceanic mixed layer. *Deep-Sea Res.* (submitted).